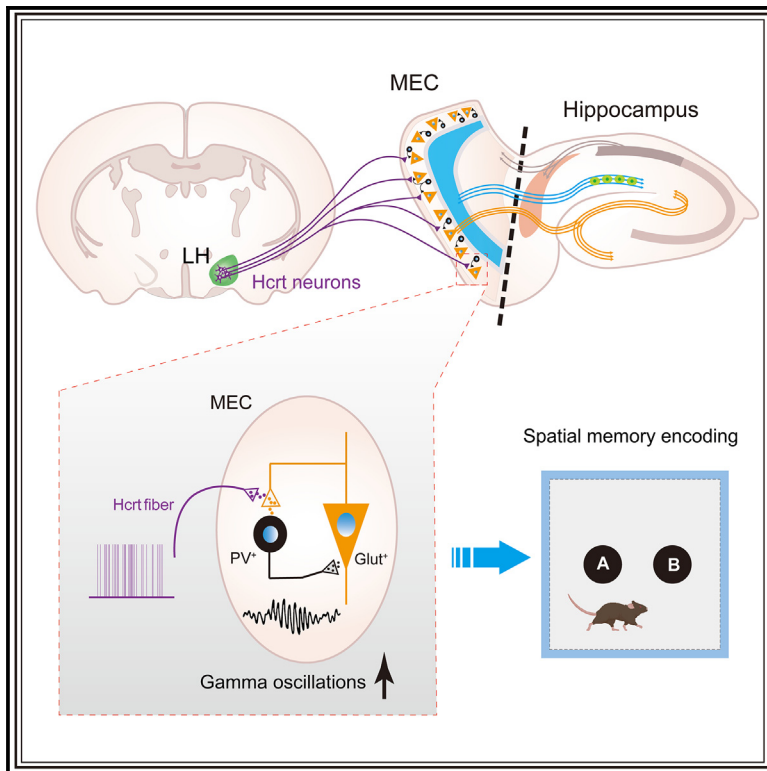# Spatial memory requires hypocretins to elevate medial entorhinal gamma oscillations

Graphical abstract

Authors

Yixiang Liao, Ruyi Wen,
Shengwei Fu, ..., Jianxia Xia, Zhian Hu,
Chao He

Correspondence

xiajxia@163.com (J.X.),
zhianhu@aliyun.com (Z.H.),
hechaochongqing@163.com (C.H.)

In brief

Liao et al. identify a pathway from the hypothalamic hypocretin neurons to the medial entorhinal cortex. They find that hypocretins act on the presynaptic glutamatergic terminals to excite parvalbumin-positive neurons in the medial entorhinal cortex and contribute to object-place memory encoding by enhancing gamma oscillations.

Highlights

- Elevation of Hcrt level in the MEC during novel object-place exploration

- A role for the LH_{Hcrt}-MEC pathway in object-place memory encoding

- Hcrt recruits presynaptic glutamatergic terminals to excite PV^+ neurons

- LH_{Hcrt}-MEC pathway supports spatial memory by tuning gamma oscillations

CellPress

Neuron

CellPress

Article

Spatial memory requires hypocretins to elevate medial entorhinal gamma oscillations

Yixiang Liao,[1,8] Ruyi Wen,[1,8] Shengwei Fu,[2] Xiaofang Cheng,[1] Shuancheng Ren,[1] Minmin Lu,[1] Ling Qian,[1] Fenlan Luo,[1] Yaling Wang,[1] Qin Xiao,[1] Xiao Wang,[1] Hengying Ye,[1] Xiaolong Zhang,[1] Chenggang Jiang,[3] Xin Li,[1] Shiyin Li,[1] Ruozhi Dang,[1] Yingying Liu,[4] Junjun Kang,[4] Zhongxiang Yao,[1] Jie Yan,[1] Jiaxiang Xiong,[1] Yanjiang Wang,[5,7] Shengxi Wu,[4] Xiaowei Chen,[6,7] Yulong Li,[2] Jianxia Xia,[1,*] Zhian Hu,[1,7,*] and Chao He[1,9,*]

[1]Department of Physiology, Institute of Brain and Intelligence, Third Military Medical University, Chongqing 400038, China
[2]State Key Laboratory of Membrane Biology, School of Life Sciences, PKU-IDG/McGovern Institute for Brain Research, Peking-Tsinghua Center for Life Sciences, National Biomedical Imaging Center, Peking University, Beijing 100871, China
[3]Department of Medical Psychology, Chongqing Health Center for Women and Children, Chongqing 400021, China
[4]Department of Neurobiology, School of Basic Medicine, Fourth Military Medical University, Xi'an, Shaanxi 710032, China
[5]Department of Neurology, Daping Hospital, Institute of Brain and Intelligence, Third Military Medical University, Chongqing 400042, China
[6]Brain Research Center, Institute of Brain and Intelligence, Third Military Medical University, Chongqing 400038, China
[7]Chongqing Institute for Brain and Intelligence, Guangyang Bay Laboratory, Chongqing 400064, China
[8]These authors contributed equally
[9]Lead contact
*Correspondence: xiajxia@163.com (J.X.), zhianhu@aliyun.com (Z.H.), hechaochongqing@163.com (C.H.)
https://doi.org/10.1016/j.neuron.2023.10.012

SUMMARY

The hypocretin (Hcrt) (also known as orexin) neuropeptidic wakefulness-promoting system is implicated in the regulation of spatial memory, but its specific role and mechanisms remain poorly understood. In this study, we revealed the innervation of the medial entorhinal cortex (MEC) by Hcrt neurons in mice. Using the genetically encoded G-protein-coupled receptor activation-based Hcrt sensor, we observed a significant increase in Hcrt levels in the MEC during novel object-place exploration. We identified the function of Hcrt at presynaptic glutamatergic terminals, where it recruits fast-spiking parvalbumin-positive neurons and promotes gamma oscillations. Bidirectional manipulations of Hcrt neurons' projections from the lateral hypothalamus (LH$_{Hcrt}$) to MEC revealed the essential role of this pathway in regulating object-place memory encoding, but not recall, through the modulation of gamma oscillations. Our findings highlight the significance of the LH$_{Hcrt}$-MEC circuitry in supporting spatial memory and reveal a unique neural basis for the hypothalamic regulation of spatial memory.

INTRODUCTION

Spatial memory is fundamental for both animals and humans in their daily lives and critically relies on the medial entorhinal cortex (MEC)-hippocampal circuit.[1–3] The processes of spatial memory, including encoding, storage, and recall, primarily take place during wakefulness. A growing body of evidence highlights the indispensable role of wakefulness-promoting systems in regulating spatial memory.[4–9] For instance, the cholinergic and monoaminergic wakefulness-promoting systems, also known as neuromodulatory systems,[10,11] directly innervate the MEC and other brain regions related to spatial memory, forming specialized neural circuits that support spatial memory through the regulation of neuronal excitability,[5,7,8] synaptic plasticity,[6,9] and synchronized activity[4,12] of memory traces. Dysfunction in these specialized neural circuits can lead to severe memory deficits, potentially underpinning clinical dysmnesia.[13–17] In addition to studying the spatial memory traces themselves, it is essential to understand how these traces are supported by various wakefulness-promoting systems.

Hypocretin (Hcrt) peptidergic neurons, located exclusively in the lateral hypothalamus (LH), constitute a prominent wakefulness-promoting system known for its critical roles in feeding, reward, and other motivated behaviors.[18–21] Clinical studies on narcoleptic patients, caused by the loss of Hcrt neurons, and animal experiments suggest that the Hcrt system may play a supporting role in various memory tasks, especially those related to spatial memory.[22–32] Pharmacological blockade of the Hcrt receptor or knockout of the Hcrt gene has been shown to impair spatial memory.[24–27,29] Conversely, elevated Hcrt signaling has been found to ameliorate memory impairment in several animal models with spatial memory deficiencies.[33–37] However, the specific role and underlying mechanisms of Hcrt neurons in supporting spatial memory remain poorly defined.

In this study, we aimed to identify the site in the spatial memory-related MEC-hippocampal circuit that is regulated by Hcrt

neurons and discovered a primary pathway from Hcrt neurons to the MEC. Using a genetically encoded G-protein-coupled-receptor-activation-based (GRAB) sensor to monitor Hcrt levels, we observed an increase in Hcrt concentration in the MEC during novel object-place exploration. This elevation in Hcrt levels correlated with enhanced gamma oscillations that support spatial memory encoding, although not recall. Gamma oscillations play a crucial role in information routing and synaptic plasticity and are essential for spatial memory.[2,38,39] Previous studies have suggested that gamma rhythmogenesis is linked to the perisomatic inhibition of glutamatergic cells.[40,41] Our findings demonstrate that Hcrt stimulates glutamatergic terminals in the MEC, leading to the excitation (Ex) of fast-spiking interneurons that enhance synchronized gamma oscillations. These results unveil a specific neuromodulatory mechanism that tunes the activity of fast-spiking interneurons, driving the gamma oscillations associated with spatial memory.

RESULTS

Hcrt neurons are engaged in novel object-place exploration and display dense innervation in the MEC

Previous studies have suggested a potential involvement of Hcrt neurons in spatial memory[24–27,29]; however, the dynamic changes in their activity during spatial memory tasks remain unresolved. To address this, we used AAV2/9-EF1α-DIO-GCaMP6f injection in Hcrt-Cre mice's LH and employed fiber photometry to specifically record compound Ca^{2+} signals from Hcrt neurons (Figure S1A). The recorded signals predominantly reflected Hcrt neuron activities, distinct from interference signals caused by locomotion, which were not detected in control mice expressing only mCherry (Figure S1B). We recorded the Ca^{2+} activity of LH Hcrt neurons during an object-place memory task that relies on the MEC.[4] During this task, two identical objects were placed in specific locations in a familiar context, and the mice explored novel locations of these objects for object-place memory encoding. The spatial distribution map of the normalized strong Ca^{2+} events was constructed within the spatial context. Remarkably, strong Ca^{2+} events were mainly observed around the locations of the two objects (Figures S1C and S1D), indicating high Hcrt neuron activation during object-place exploration.

Further analysis of the dynamic changes in Ca^{2+} signals when mice approached the object area each time at this encoding stage. According to a previous study,[42] we defined an onset time of the object-place exploration, when the mouse head entered the area with a radius of 3 cm around the border of objects. When mice approached the location of object A or object B, Ca^{2+} activities of the Hcrt neurons remarkably increased (Figures S1E–S1H). The 405-nm isosbestic control channel showed no apparent signal changes when animals explored objects A and B (Figure S1I). No significant difference between the time spent in exploring object A and object B was observed, reflected by the fact that the discrimination index was not significantly greater than zero (Figure S1J). Furthermore, we found no significant increase in Ca^{2+} activity when the mice simply turned their heads toward object A and object B and did not enter the area around the object to explore (Figures S1K and S1L).

Furthermore, we conducted another behavioral task in which object B was moved to a novel location 5 min after the mice explored the original locations of objects A and B (Figure S2A). Since the mice have already encoded the location of object A, they would show a preference for object B and encode the novel place of this object at the recall stage. Under this condition, Hcrt neurons indeed exhibited stronger Ca^{2+} signal activity when mice explored the location of object B, whereas no significant change was observed when mice explored the location of object A (Figures S2A and S2B). Additionally, mice spent more time exploring object B than object A and displayed a discrimination index greater than zero (Figure S2C), indicating their preference for encoding the novel object location. In contrast, no obvious signal changes were observed in the 405-nm isosbestic control channel when animals explored the locations of objects A and B (Figure S2D).

Compared with the encoding stage, the Ca^{2+} signal activity of Hcrt neurons recorded during the exploration of the familiar location of object A decreased, whereas the signals recorded during the exploration of the novel location of object B still remained at a high level at the recall stage (Figure S2E). These results suggest that Hcrt neurons are activated during exploration of the novel, but not the familiar, locations of the object.

To determine whether Hcrt neurons are specifically involved in the object-place memory task, we further detected the changes in Hcrt neuron activity during the animals' first exposure to an environment with and without novel objects (Figure S2F). During animals' first exposure to an environment without novel objects, mice exhibited stillness and exploratory movement. The activation of Hcrt neurons was observed during active exploration behavior (Figures S2G and S2H). Then, two objects were placed in the explored environment. We consistently observed that Hcrt neurons were activated during object-place exploration (Figures S2I and S2J). When comparing the degree of Hcrt neuronal activation under these two conditions, we found that Hcrt neurons exhibited higher activities during object-place exploration than during the initial exploration of the environment without objects (Figure S2K), indicating that Hcrt neurons are specifically involved in object-place exploration, but not only function as a novelty detector of the environment.

Given the activation of Hcrt neurons during novel object-place exploration, it is plausible that they detect object-place novelty and influence the activity of brain regions crucially involved in novel object-place memory formation, including the MEC and hippocampus.[3,43] To assess how Hcrt neurons affect the MEC-hippocampal circuit, we mapped c-Fos expression in the hippocampus and MEC upon chemogenetic activation of Hcrt neurons. We injected AAV2/9-EF1α-DIO-hM3D (Gq)-mCherry into the LH of Hcrt-Cre mice and administered an intraperitoneal injection of clozapine-N-oxide (CNO, 1 mg/kg) (Figure 1A). Immunohistochemical staining confirmed specific hM3D-mCherry expression in Hcrt neurons, with most Hcrt neurons showing c-Fos expression 2 h after CNO administration, indicating *in vivo* activation of Hcrt neurons (Figure 1B). Notably, c-Fos-positive cells were significantly increased in the MEC and slightly increased in cornu ammonis 3 (CA3), but no significant changes were observed in most other hippocampal subregions (Figures 1C and 1D).

CellPress
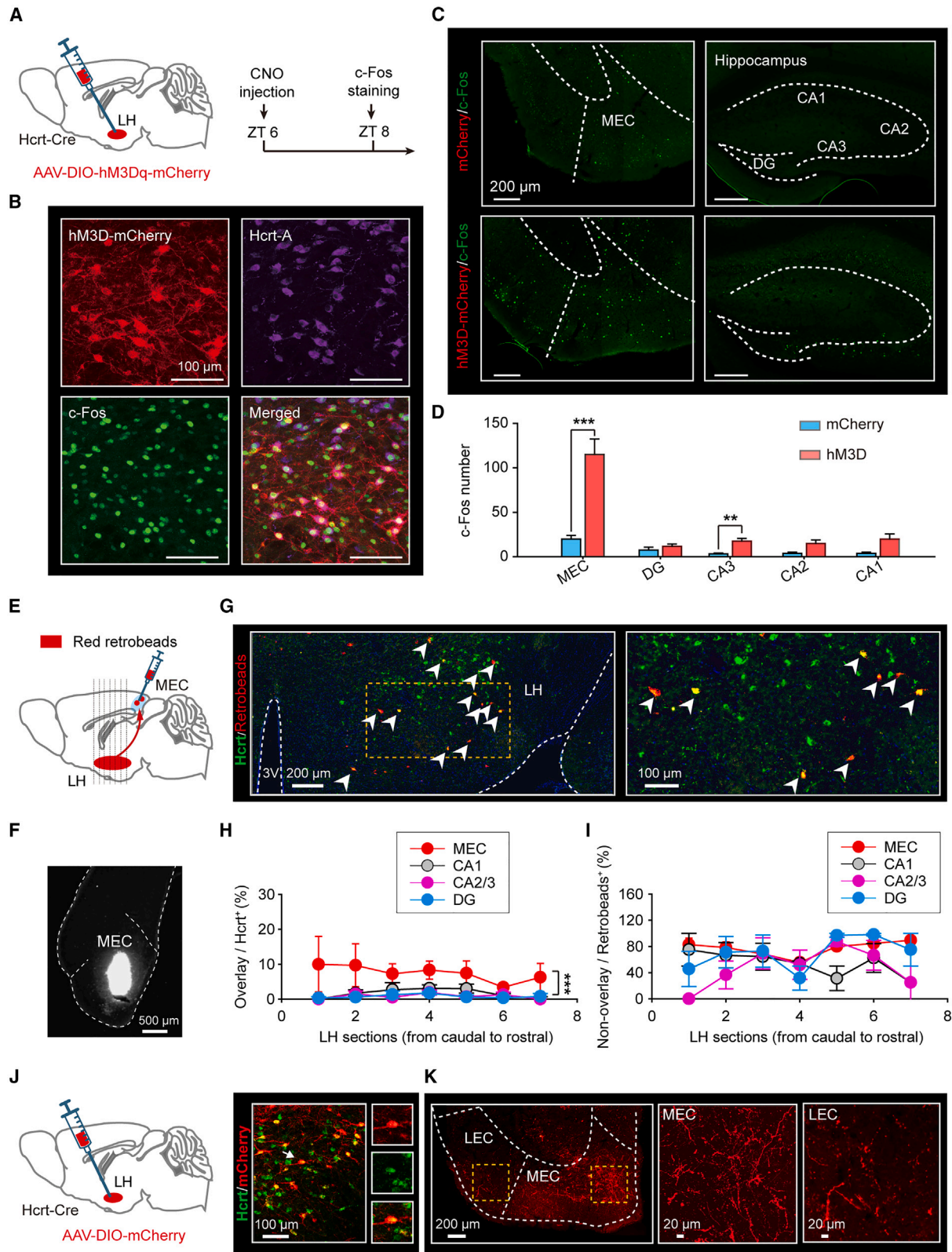
Furthermore, we investigated whether Hcrt neurons establish direct connections with the MEC. We employed a chemical-based retrograde-tracing method by injecting red retrobeads into the MEC (Figures 1E and 1F). The somata of red retrobead-labeled neurons were observed in the LH (Figure 1G). Immunohistochemical staining for Hcrt-A peptide confirmed that 27% of the retrogradely labeled neurons expressed this peptide, confirming direct connections between Hcrt neurons and the MEC. These retrogradely labeled Hcrt neurons that projected to the MEC were broadly distributed in the LH (Figure 1H). We also injected the red retrobeads into the different subregions of the hippocampus, including CA1, CA2/CA3, and dentate gyrus (DG), and the neighboring brain structures of the MEC such as the lateral entorhinal cortex, postrhinal cortex, and subiculum. We found that the percentage of these retrogradely labeled MEC-projecting Hcrt neurons to the total Hcrt neurons was highest compared with the different subregions of the hippocampus and the neighboring brain structures of the MEC (Figures 1H and S3A–S3E). However, there were no significant differences in the proportion of retrogradely labeled non-Hcrt neurons in the LH that projected the MEC and other brain regions in the overall retrograde labeled cells (Figures 1I and S3F).

Additionally, we conducted anterograde tracing by injecting AAV2/9-EF1α-DIO-mCherry into the LH of Hcrt-Cre mice. Immunohistochemical staining confirmed mCherry-specific expression in Hcrt neurons (Figure 1J). Interestingly, the superficial layers of the MEC exhibited a high density of mCherry fibers (Figure 1K). Compared with the density of Hcrt fibers in the different subregions of the hippocampus and these neighboring areas of the MEC, the highest density of Hcrt fibers was detected in the MEC (Figure S4). Together, these results suggest that MEC receives the prominent inputs of Hcrt neurons in the MEC-hippocampal circuit.

Elevation of Hcrt level in the MEC during novel object-place exploration

To precisely monitor extracellular Hcrt levels with high specificity and temporal resolution, we developed a genetically encoded GRAB sensor for Hcrt (Figure 2A). The GRAB Hcrt sensor was engineered by replacing the third intracellular loop in the Hcrt receptor type 2 (HCRTR2) with a circularly permutated EGFP (cpEGFP) from a previously developed GRAB norepinephrine (NE) sensor.[44] Based on the previous experience in developing GRAB sensors,[44–49] and the novel strategy for accelerating the development of GRAB sensors for neuropeptides,[50] we further optimized prototype reported in our previous study[50] and identified variant, termed $GRAB_{Hcrt0.5}$, with nanomolar affinity and a substantial fluorescence response ($\Delta F/F_0$). When expressed in cultured neurons, $GRAB_{Hcrt0.5}$ demonstrated efficient plasma membrane trafficking and stable detection of extracellular Hcrt levels, as evidenced by no significant decrease in fluorescence when exposed to Hcrt-A (10 μM) for 2 h (Figures 2B and 2C). Additionally, $GRAB_{Hcrt0.5}$ exhibited dose-dependent responses to Hcrt-A and Hcrt-B, with a maximum $\Delta F/F_0$ of approximately 1,100% and half maximal effective concentration (EC_{50}) values of 210 and 100 nM, respectively (Figure 2D). Specificity testing confirmed that $GRAB_{Hcrt0.5}$ responded exclusively to Hcrt, and not to various neurotransmitters and neuromodulators. Notably, the Hcrt-induced responses in $GRAB_{Hcrt0.5}$ were blocked by the Hcrt receptor antagonist (Figure 2E). Moreover, $GRAB_{Hcrt0.5}$ displayed similar Ex and emission (Em) spectra as EGFP under one-photon Ex (Figure 2F). Compared with another genetically encoded Hcrt sensor OxLight1,[51] $GRAB_{Hcrt0.5}$ exhibited similar affinity but approximately ~5-fold higher maximum brightness (Figure S5).

With the newly developed $GRAB_{Hcrt0.5}$ sensors, we examined the dynamic release of endogenous Hcrt in the MEC during the object-place memory task. We injected AAV2/9 expressing $GRAB_{Hcrt0.5}$ under the control of the human synapsin (hSyn) promoter and implanted optical fibers in the MEC (Figure 2G). Objects A and B were placed in specific locations in the familiar context (Figure 2H). To eliminate motion artifacts, we presented the corrected 488-nm fluorescence signals obtained by subtracting the 405-nm isosbestic raw trace from the 488-nm raw trace. There was no significant difference between the time the mice spent exploring object A and object B at this encoding stage, and the discrimination index was not significantly greater than zero (Figure 2I). Remarkably, when mice approached the

Figure 1. Innervation of the MEC by hypocretin neurons
(A) Schematic of the CNO injection and immunohistochemical staining for c-Fos.
(B) Confocal images showing hM3D-mCherry (red), and immunohistochemical staining for Hcrt-A (purple) and c-Fos (green) after intraperitoneal infusion of CNO.
(C) Images showing c-Fos expression levels in the MEC and the different subregions of the hippocampus after CNO injection in the mCherry (top) or hM3D (bottom) groups. The images of the MEC were composites and constructed from two adjacent images from the same brain sections.
(D) Bar graphs showing the number of c-Fos positive neurons in the different subregions of the entorhinal cortex and hippocampus. MEC, medial entorhinal cortex. DG, dentate gyrus (MEC: unpaired t test, n = 5 mice, p < 0.001; DG: unpaired t test, n = 5 mice, p = 0.38; CA3: unpaired t test, n = 5 mice, p < 0.01; CA2: Mann-Whitney rank sum test, n = 5 mice, p = 0.06; CA1: Mann-Whitney rank sum test, n = 5 mice, p = 0.06). Bar graphs show mean ± SEM.
(E) Schematic of the red retrobead-mediated retrograde tracing.
(F) A representative image showing that red retrobeads were solely injected into the MEC.
(G) Overlay of the red retrobeads with Hcrt-A (green) in the LH. Right panels show an enlarged view of the double-labeled neurons as indicated by arrowheads.
(H) Percentage of double-labeled cells to the total Hcrt cells from rostral to caudal in the LH (Scheirer-Ray-Hare test, n = 4 mice for each group, brain region factor: p < 0.001, LH section factor: p < 0.01, interaction: p = 0.99). Data are represented as mean ± SEM.
(I) Percentage of red retrobead-labeled Hcrt-negative cells to the total red retrobead-positive cells in the LH (two-way RM ANOVA, n = 4 mice for each group, p = 0.22). Data are represented as mean ± SEM.
(J) Schematic showing mCherry-mediated anterograde tracing (left). An image showing mCherry (red) and immunohistochemical staining for Hcrt-A (green) in the LH (right).
(K) A representative image illustrating mCherry expression in the entorhinal cortex. The image in the left was a composite and constructed from the same brain sections.
See Table S1 for full results of statistical tests.
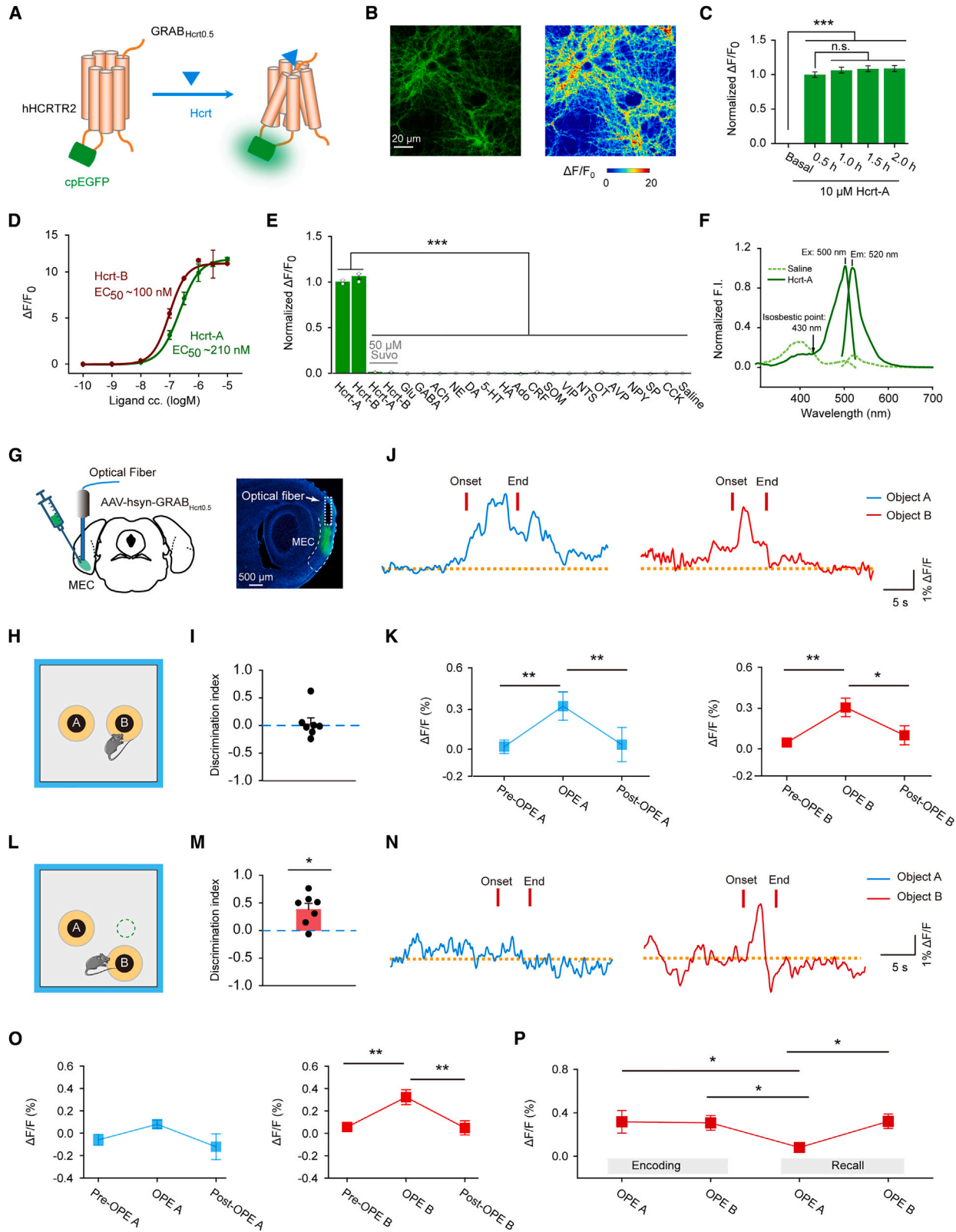
(legend on next page)

location of object A or object B at the encoding stage, the fluorescence signal reflecting endogenous Hcrt release increased significantly (Figures 2J and 2K). Additionally, no significant changes in Hcrt release were observed when the mice merely turned their heads toward object A and object B without approaching the area around these objects (Figures S6A and S6B).

To confirm that this elevation of Hcrt was specific to the exploration of the novel location of the object, we moved object B to a novel location 5 min after these mice explored the original locations of objects A and B (Figure 2L). Under this condition, mice showed a preference for encoding the novel location of object B (Figure 2M). Consistently, elevation of Hcrt release was observed only when mice explored the location of object B, but not object A, at this recall stage (Figures 2N and 2O). In addition, compared with the encoding stage, the fluorescence signal recorded during the exploration of the familiar location of object A became smaller, but the signals recorded during the exploration of the novel location of object B still remained at a high level at the recall stage (Figure 2P). These results suggest that Hcrt levels in the MEC are elevated during the exploration of the novel location of the object.

To further validate these findings, we conducted another experiment involving mice going through five contextual exposure sessions. Mice were initially placed in a novel square enclosure containing two objects for 5 min (S1). Following a 5-min intersession interval, mice were returned to the same context for three additional 5-min sessions (S2, S3, and S4) with 5-min intervals. After familiarization with the locations of the objects over these four habituation sessions (S1–S4), objects A and B were both placed in novel locations during session S5 (Figure S6C). After four habituation sessions (S1–S4), the time spent in the object-place exploration decreased (Figure S6D), indicating familiarization with the object-place. The increase of signal intensity also gradually decreased. Strikingly, Hcrt release again was increased when the mice explored the novel locations of objects A and B during session S5 (Figures S6E and S6F). Together, these data indicate increased Hcrt release during novel object-place exploration.

Next, we assessed the changes in Hcrt release in the MEC during the animals' first exposure to an environment with or without novel objects (Figure S6G). In environments without objects, Hcrt release in the MEC has a tendency to increase during active exploration behavior (Figures S6H and S6I). During object-place exploration, a higher elevation of Hcrt levels in the MEC was observed compared with the first exploration in the environment without objects (Figures S6J–S6L), implying that the Hcrt release in the MEC indeed is associated with object-place exploration.

A role for the LH$_{Hcrt}$-MEC pathway in object-place memory encoding

The primary objective of this study was to elucidate how Hcrt neurons contribute to spatial memory support. Given the increase in Hcrt levels in the MEC during novel object-place exploration, we redirected our focus to investigate the role of Hcrt neuron projections to the MEC as potential mediators of this support. To selectively inhibit the LH$_{Hcrt}$-MEC pathway, we administered AAV2/9-EF1α-DIO-hM4D (Gi)-mCherry into the LH of Hcrt-Cre mice, combined with local infusion of CNO (5 μM) into the MEC (Figure 3A). Immunohistochemical staining confirmed the

Figure 2. Hcrt increases in the MEC during novel object-place exploration

(A) Schematic of the principle behind the GRAB$_{Hcrt0.5}$ sensors in which cpEGFP is inserted within the human Hcrt receptor type 2 (hHCRTR2). Upon binding to the Hcrt, the resulting conformational change of hHCRTR2 induces increases in fluorescence.

(B) Representative image of cultured neurons expressing GRAB$_{Hcrt0.5}$ in responses to Hcrt perfusion.

(C) Normalized fluorescence response to Hcrt perfusion for 2 h (one-way ANOVA, n = 30 cells for each group, p < 0.001). Data are represented as mean ± SEM.

(D) Dose-response curves measured in HEK293T cells expressing GRAB$_{Hcrt0.5}$. Corresponding EC$_{50}$ values for Hcrt-A and Hcrt-B are shown.

(E) Bar graphs with overlaid dot plots showing the normalized fluorescence change measured in HEK293T cells expressing GRAB$_{Hcrt0.5}$ in response to Hcrt alone, Hcrt together with the Hcrt receptor antagonist (suvorexant), and other neurotransmitters and neuromodulators (one-way ANOVA, n = 3 wells per group with 300–500 cells per well, p < 0.001). Glu, glutamate; GABA, γ-aminobutyric acid; ACh, acetylcholine; NE, norepinephrine; DA, dopamine; 5-TH, serotonin; HA, histamine; Ado, adenosine; CRF, corticotropin-releasing factor; SOM, somatostatin; VIP, vasoactive intestinal polypeptide; NTS, neurotensin; OT, oxytocin; AVP, arginine vasopressin; NPY, neuropeptide Y; SP, substance P; CCK, cholecystokinin. Data are represented as mean ± SEM.

(F) One-photon excitation (Ex) and emission (Em) spectra of GRAB$_{Hcrt0.5}$ measured in the absence and presence of Hcrt.

(G) Schematic depicting the strategy for fiber photometry recording of GRAB$_{Hcrt0.5}$ fluorescence (left). An image showing the expression of GRAB$_{Hcrt0.5}$ in the MEC (right).

(H) Schematic depicting the fiber photometry recording of GRAB$_{Hcrt0.5}$ fluorescence in the MEC of freely behaving mice during the object-place exploration task.

(I) Discrimination index for mice exploring objects A and B during the encoding phase (one-sample signed rank test, n = 7 mice for each group, p = 0.84). Data are represented as mean ± SEM.

(J) Examples of fluorescence signals before, during, and after object-place exploration of the encoding phase.

(K) Fluorescence signals before, during, and after object-place exploration of the encoding phase (one-way RM ANOVA, n = 7 mice for each group, p < 0.01, left; one-way RM ANOVA, n = 7 mice for each group, p < 0.01, right). Data are represented as mean ± SEM.

(L) Schematic showing the design of the object-place memory task, where after the mice explored the locations of objects A and B, the spatial position of object B was changed.

(M) Discrimination index for mice exploring objects A and B during the recall phase (one-sample t test, n = 7 mice for each group, p < 0.05). Data are represented as mean ± SEM.

(N) Examples of fluorescence signals before, during, and after object-place exploration of the recall phase.

(O) Fluorescence signals before, during, and after exploring objects A and B of the recall phase (one-way RM ANOVA, n = 7 mice for each group, p = 0.08, left; one-way RM ANOVA, n = 7 mice for each group, p < 0.01, right). Data are represented as mean ± SEM.

(P) A comparison of the fluorescence signals during exploring objects A and B between the encoding and recall phases (one-way RM ANOVA, n = 7 mice for each group, p < 0.05). Two mice were excluded for incorrect location of optical fibers and one mouse was excluded for lack of exploratory motivation. Seven mice were shared in the (G)–(P) and Figure S6B. Data are represented as mean ± SEM.
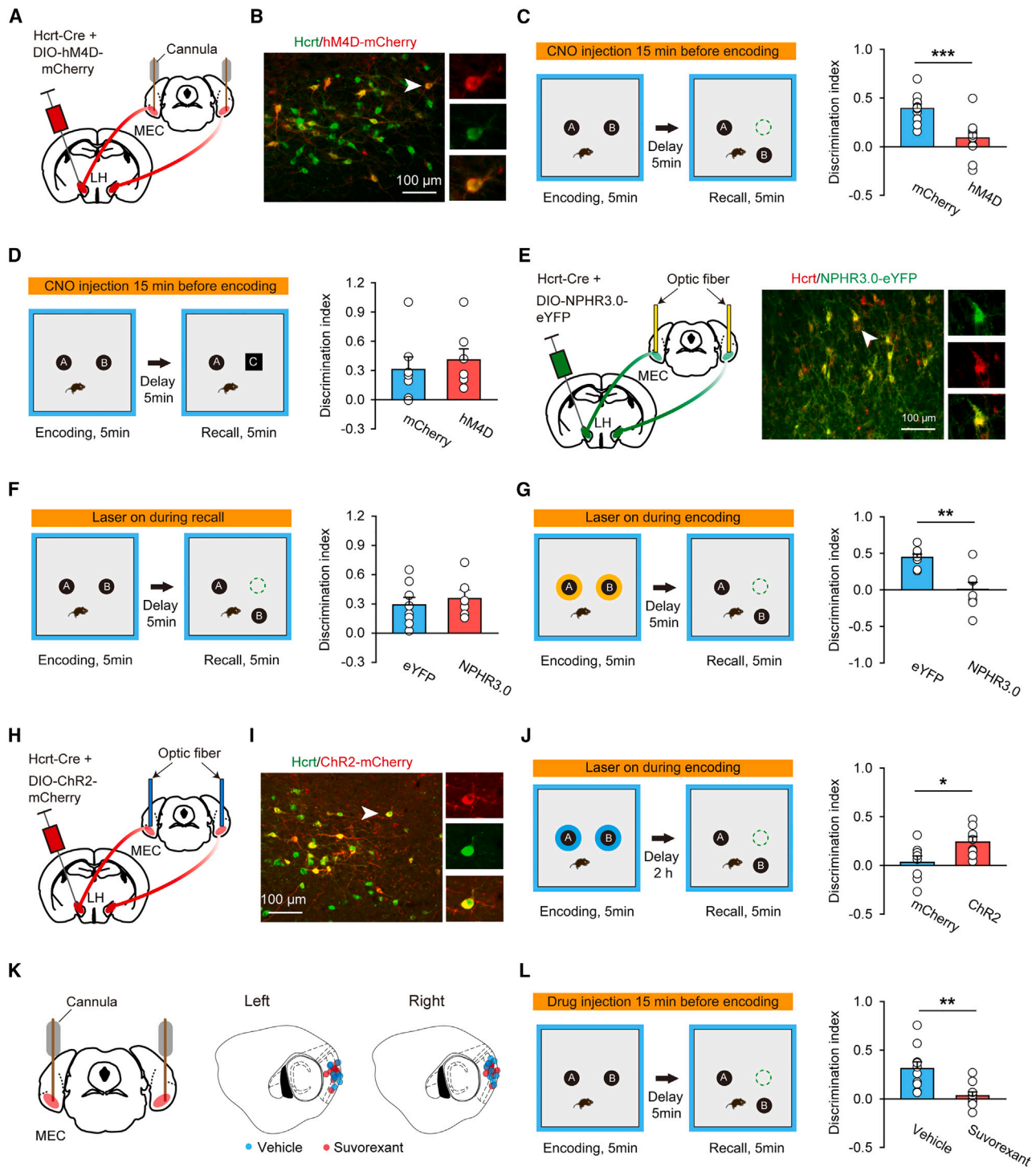
See Table S1 for full results of statistical tests.

Figure 3. LH$_{Hcrt}$-MEC pathway is involved in the object-place memory encoding, but not the recall

(A) Schematic of chemogenetic inhibition of the LH$_{Hcrt}$-MEC pathway.

(B) An image showing hM4D-mCherry (red) and immunohistochemical staining for Hcrt-A (green).

(C) Effects of chemogenetic inhibition of LH$_{Hcrt}$-MEC pathway on object-place memory encoding (unpaired t test, mCherry: n = 11 mice; hM4D: n = 13 mice, p < 0.001). Two mice were excluded for incorrect location of cannula. Data are represented as mean ± SEM.

(D) Effects of chemogenetic inhibition of LH$_{Hcrt}$-MEC pathway on novel object memory (Mann-Whitney rank sum test, n = 7 mice for each group, p = 0.46). Two mice were excluded for incorrect location of cannula. Data are represented as mean ± SEM.

specific expression of hM4D-mCherry in Hcrt neurons (Figure 3B). Whole-cell recordings from brain slices demonstrated that CNO effectively inhibited hM4D-expressing Hcrt neurons (Figures S7A–S7C). Local CNO infusion in the MEC prior to object-place exploration impaired the mice's ability to recognize the changed spatial position of object B, leading to a decrease in the discrimination index during the recall stage (Figures 3C, S7D, and S7E). Chemogenetic inhibition of the LH$_{Hcrt}$-MEC pathway did not affect the traveling distance in the object-place memory task, indicating that the observed memory impairment might be not caused by the lack of explorative motivation (Figures S7F and S7G).

To further investigate whether this pathway is specifically involved in object-place memory, we performed a novel object memory task, which is dependent on the lateral entorhinal cortex, an adjacent brain region of MEC.[4] Mice were first allowed to explore the locations of two identical objects in a familiar context for 5 min. During the recall stage, object B was replaced by another novel object C, but its location remained unchanged. The control mice expressing mCherry exhibited novel object memory as evidenced by their preference for the novel object C compared with the familiar object A. Chemogenetic inhibition of the LH$_{Hcrt}$-MEC pathway did not change the discrimination index in the novel object task (Figure 3D). These results suggest that the LH$_{Hcrt}$-MEC pathway is selectively involved in object-place memory, and the local CNO injection to manipulate LH$_{Hcrt}$-MEC pathway would not affect behaviors related to the adjacent brain regions of the MEC.

It has been reported that CNO could be converted into its metabolite clozapine, which has hM4D-independent side-effects on behaviors in wild-type mice upon systemic injections.[52–54] We further performed control experiments in which CNO was locally injected into the MEC of wild-type mice (Figures S8A–S8C). Under this condition, CNO injections did not affect the object-place memory encoding and traveling distance (Figure S8D), implying that the changes in the object-place memory were indeed due to CNO-mediated inhibition of the LH$_{Hcrt}$-MEC pathway.

Since it takes at least 10 min for CNO to maximize its effect through diffusion, the stage of object-place memory at which this pathway operates is still unclear. To test this, we performed optogenetic inhibition of the LH$_{Hcrt}$-MEC pathway at different stages. Optogenetic interventions were performed by expressing the inhibitory natronomonas pharaonis halorhodopsin (NpHR) fused to enhanced yellow fluorescent protein (eYFP) or eYFP alone in the Hcrt neurons as a control. The specificity of NpHR expression in the Hcrt neurons was confirmed by immunohistochemical staining (Figure 3E). Multi-channel single-unit recordings showed that yellow light (589 nm) potently inhibited NpHR-expressing neurons (Figures S9A–S9D). Optogenetic inhibition of the LH$_{Hcrt}$-MEC pathway at the recall stage did not affect the discrimination index (Figure 3F). Additionally, no significant difference was observed in the traveling distance between the NpHR and eYFP groups at the encoding stage (Figures S9E and S9F). These data suggest that the LH$_{Hcrt}$-MEC pathway is not required for object-place memory recall.

Considering the significant activation of Hcrt neurons during the exploration of novel object locations, we further explored the behavioral effects of optogenetic manipulation of the LH$_{Hcrt}$-MEC pathway within a specific subarea around the objects during the encoding stage. Real-time tracking of the animal's body center allowed us to deliver yellow light to inhibit the LH$_{Hcrt}$-MEC pathway through two implanted optical fibers when the mice explored within a marked subarea around the objects (10 cm away from the center of the object) (Figures S9G–S9I). The average total durations of optogenetic intervention were 30.3 and 28.9 s, and the percentage of optogenetic inhibition time in objects A and B zone was 69% and 70% for the eYFP and NpHR groups, respectively (Figure S9J). The mice with optogenetic inhibition of the LH$_{Hcrt}$-MEC pathway could not recognize a changed spatial position of object B and displayed a decrease in the discrimination index with the traveling distance unaffected (Figure S9K).

Although animal body center tracking is commonly used,[42,55] it can trigger optogenetic stimulations when the animal's body passes over the objects instead of actually exploring the objects' locations. Therefore, we further improved the video-tracking system by installing light-emitting diodes on the head of the mouse. Thus, it was made possible to track the head of the mouse specifically, allowing the head to enter 3 cm around the border of these objects to trigger optogenetic interventions (Figures 3G and S9L). Under this condition, the percentage of optogenetic inhibition time in object A and object B zones reached 89% and 91% for the eYFP and NpHR groups, respectively (Figure S9M). Consistently, we also found that optogenetic inhibition of the LH$_{Hcrt}$-MEC pathway impaired the object-place memory encoding, as reflected by a decrease in the discrimination index with traveling distance unaffected (Figures 3G and S9N).

(E) Schematic of optogenetic inhibition of the LH$_{Hcrt}$-MEC pathway (left). An image showing NpHR-eYFP (green) and immunohistochemical staining for Hcrt-A (red) (right).

(F) Effects of optogenetic inhibition of LH$_{Hcrt}$-MEC pathway on object-place memory recall (unpaired t test, eYFP: n = 8 mice, NpHR: n = 6 mice, p = 0.58). Data are represented as mean ± SEM.

(G) Effects of closed-loop optogenetic inhibition of LH$_{Hcrt}$-MEC pathway on the object-place memory encoding when the heads of the animals enter the surrounding area of the objects (unpaired t test, n = 8 mice for each group, p < 0.01). Data are represented as mean ± SEM.

(H) Schematic of optogenetic activation of the LH$_{Hcrt}$-MEC pathway.

(I) An image showing ChR2-mCherry (red) and immunohistochemical staining for Hcrt-A (green).

(J) Effects of closed-loop optogenetic activation of the LH$_{Hcrt}$-MEC pathway on the object-place memory encoding when the heads of animals enter the surrounding area of the objects (unpaired t test, n = 8 mice for each group, p < 0.05). Data are represented as mean ± SEM.

(K) Schematic of the administration Hcrt receptor blockers in the MEC (left). Reconstruction of the microinjection sites for all tested mice (right).

(L) Effects of local infusion of the Hcrt receptor antagonists in the MEC on object-place memory (unpaired t test, n = 10 mice for each group, p < 0.01). Two mice were excluded for incorrect location of cannula and two mice were excluded for lack of exploratory motivation. Data are represented as mean ± SEM.

See Table S1 for full results of statistical tests.

Neuron
Article

CellPress

In addition, we optogenetically activated the LH$_{Hcrt}$-MEC pathway in object-place memory tasks. The channelrhodopsin-2 fused with mCherry (ChR2) or mCherry alone was expressed in the Hcrt neurons and LH$_{Hcrt}$-MEC projections were stimulated during spatial memory encoding (Figure 3H). The specificity and effectiveness of ChR2 in the Hcrt neurons were confirmed by immunohistochemical staining (Figure 3I) and multi-channel single-unit recordings *in vivo* (Figures S10A and S10B), respectively. During the memory encoding session, mouse exploration within a marked subarea about 10 cm away from the center of the object triggered the delivery of blue light (470 nm) pulses to stimulate the LH$_{Hcrt}$-MEC pathway by tracking the animal's body center (Figures S10C–S10E). The average total durations of optogenetic stimulation were 38.3 and 35.1 s, and the percentages of optogenetic stimulation time in object A and object B zones were 72% and 79% for the ChR2 and mCherry groups, respectively (Figure S10F). This manipulation prolonged the duration of the mice's object-place memory to 2 h with expression of ChR2, but not in the control mice with expression of mCherry (Figure S10G). The traveling distance was not affected by the activation of the LH$_{Hcrt}$-MEC pathway (Figure S10H).

Furthermore, we tracked the head of the mouse in real time, and optogenetic stimulation was triggered when the head of the mice entered 3 cm around the border of the object (Figures 3J and S10I). The percentage of optogenetic stimulation time in object A and object B zones reached 89% and 96% for the ChR2 and mCherry groups, respectively (Figure S10J). Indeed, the duration of the object-place memory was prolonged after the optogenetic activation of the LH$_{Hcrt}$-MEC pathway during the encoding stage (Figures 3J and S10K). Even if the heads of the mice were tracked to trigger the optogenetic interventions, it is still possible that optogenetic interventions were administered when the animal's head simply passed through rather than actually explored the location of the objects. Nonetheless, these results suggest that the activation of Hcrt neurons around the object zone promotes object-place memory encoding.

Finally, we investigated whether blocking Hcrt receptors in the MEC affects object-place memory. Suvorexant, an Hcrt receptor antagonist, was administered before object-place memory encoding (Figure 3K). The mice with Hcrt receptor blockade in the MEC also exhibited impaired recognition of the changed spatial position of object B, leading to a decrease in the discrimination index (Figure 3L). These findings provide evidence that Hcrt receptor activation in the MEC is essential for object-place memory.

Hcrt recruits presynaptic glutamatergic terminals to excite PV$^+$ neurons, unlike other wakefulness-promoting neurotransmitters

Having established the causal role of the LH$_{Hcrt}$-MEC pathway in object-place memory, our next focus was to investigate the cellular mechanisms underlying this pathway's support in object-place memory. Initial recordings from excitatory glutamatergic neurons in the superficial layers of the MEC on brain slices did not reveal any direct effects of Hcrt-A peptide on membrane potentials after blocking glutamatergic and GABAergic synaptic transmissions (Figures 4A and 4B). We further examined spontaneous miniature excitatory postsynaptic currents (mEPSCs) and miniature inhibitory postsynaptic currents (mIPSCs) from glutamatergic neurons, finding that Hcrt-A did not affect the amplitude and frequency of these currents (Figures S11A and S11B). These results suggest that Hcrt does not directly influence the excitability of glutamatergic neurons in the superficial layers of the MEC.

The activity of glutamatergic neurons in the superficial layers of the MEC is tightly regulated by surrounding GABAergic neurons.[56] We recorded spontaneous inhibitory postsynaptic currents (SIPSCs) from excitatory neurons with V$_m$ at +10 mV, close to the reversal potential of ionotropic glutamate (Glu) receptors, without general blockade of excitatory synaptic transmissions. Under this condition, Hcrt dramatically increased the amplitude and frequency of SIPSCs in glutamatergic neurons, suggesting an increase in GABAergic neuron activity (Figures 4C–4E). Subsequently, we directly recorded GABAergic neurons to investigate the effects of Hcrt on these neurons, distinguishing two main types of GABAergic neurons based on their electrophysiological characteristics: fast-spiking putative parvalbumin-positive (PV$^+$) neurons and non-fast-spiking putative somatostatin-positive (SOM$^+$) neurons.

Consistent with the previous findings,[56] these two types of interneurons exhibited distinct intrinsic properties. Compared with the SOM$^+$ interneurons, PV$^+$ interneurons have lower input resistance, smaller voltage sags induced by hyperpolarizing current pulses, higher rheobase, and greater after-hyperpolarization (Figure S11C). A different firing behavior and a low-threshold spiking feature were observed for the SOM$^+$ interneurons (Figures S11D and S11E). Application of Hcrt only decreased the rheobase of PV$^+$ interneurons without influencing other intrinsic properties (Figure S11F). No significant changes in the intrinsic properties of SOM$^+$ interneurons were observed after the application of Hcrt (Figure S11G). However, bath application of Hcrt-A strongly increased firing rates of fast-spiking PV$^+$ interneurons (Figures 4F and 4G). Although Hcrt-A just slightly increased the firing rates of non-fast-spiking SOM$^+$ neurons, this effect was much weaker than that of the fast-spiking PV$^+$ interneurons (Figures S12A–S12C). Additionally, a series of inward currents were injected to mimic the excitatory inputs *in vivo* and make interneurons fire at a frequency close to gamma frequency. Under this condition, bath application of Hcrt peptide significantly increased the firing frequency of PV$^+$ interneurons while SOM$^+$ interneurons remained unaffected (Figures 4H and S12D). Taken together, these results indicate that Hcrt primarily excites GABAergic interneurons, particularly exerting strong excitatory effects on fast-spiking PV$^+$ interneurons.

We then further explored the mechanisms underlying Hcrt-induced Ex of the PV$^+$ neurons. Hcrt-A-induced Ex of the fast-spiking PV$^+$ neurons could be blocked by either Hcrt 1 receptor antagonist (Figure S12E) or the ionic glutamatergic receptor antagonists (Figure S12F). Additionally, application of Hcrt-A peptide increased the amplitude but did not alter the frequency of the spontaneous excitatory postsynaptic currents (SEPSCs) in the fast-spiking PV$^+$ neurons (Figure S12G), indicating that the Hcrt-A-induced Ex of the fast-spiking PV$^+$ cells was an indirect effect caused by enhancing excitatory synaptic inputs on the fast-spiking PV$^+$ cells. To test whether Hcrt functions at presynaptic terminals or affects postsynaptic glutamatergic receptors, we recorded mEPSCs of the fast-spiking PV$^+$ neurons after

Neuron
Article
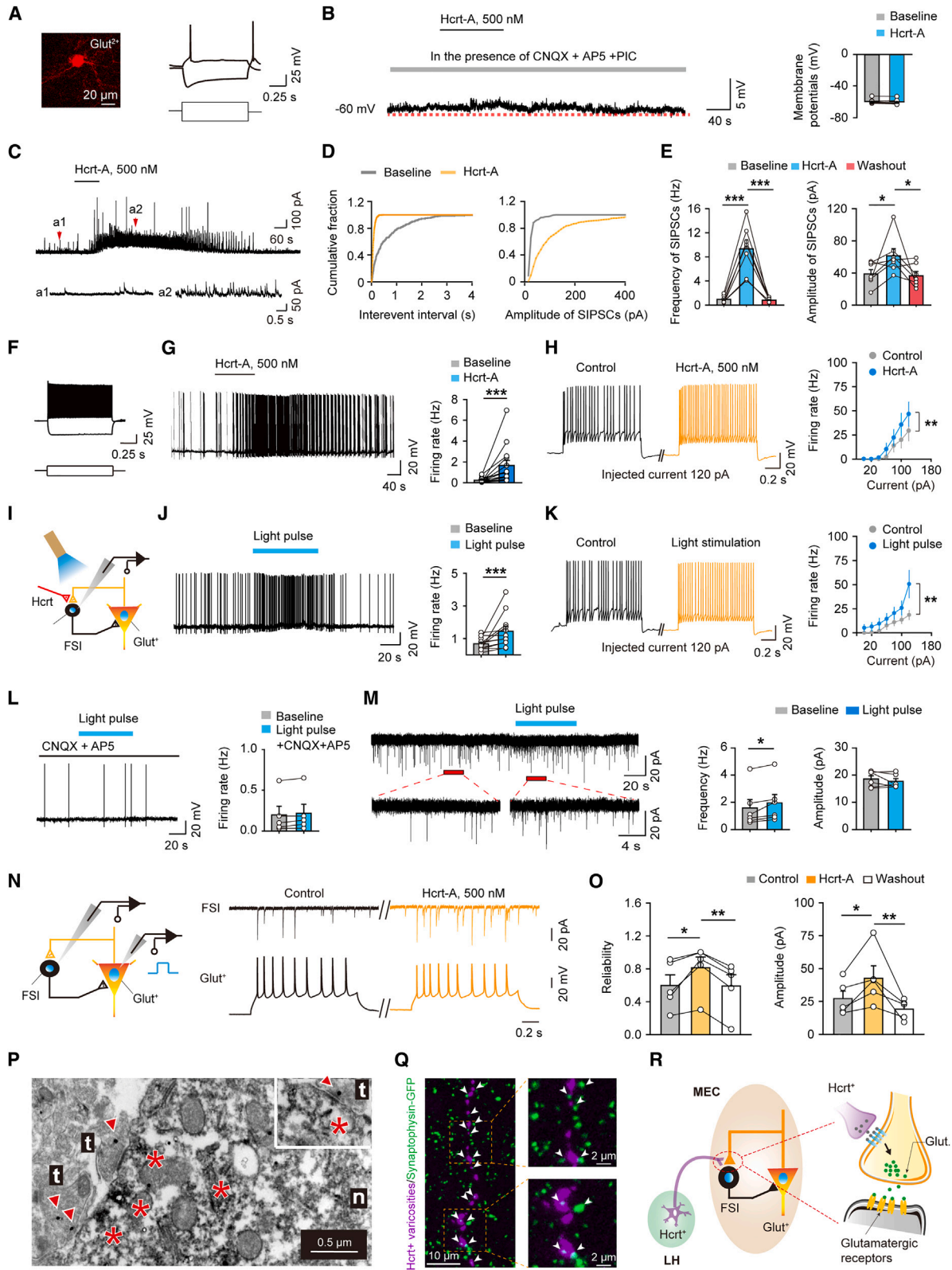
(legend on next page)

blocking voltage-gated Na^+ channels. A change in the amplitude of mEPSCs represents a postsynaptic effect, whereas an alteration in the frequency reflects a change in the presynaptic release.[7] The application of Hcrt-A enhanced the frequency without affecting the amplitude of mEPSCs (Figure S12H), suggesting that Hcrt enhances the Glu release from the presynaptic terminals to excite fast-spiking PV^+ neurons.

We also investigated the effects of endogenous Hcrt evoked by optogenetic stimulation of Hcrt fibers in the MEC (Figure 4I). Consistently, optogenetic stimulation of Hcrt fibers activated fast-spiking PV^+ neurons (Figure 4J). Upon injections of a series of inward currents to evoke the action potentials of PV^+ neurons, optogenetic stimulation of Hcrt fibers also significantly accelerated the firing frequency of these neurons. When a 120 pA inward current was injected, the firing frequency of PV^+ interneuron was remarkably increased from below the gamma frequency band (18.5 ± 4.83 Hz) to the gamma frequency band (50.67 ± 14.34 Hz) (Figure 4K). Although co-release of Hcrt and Glu neurotransmitters from Hcrt neurons has been reported,[57] the excitatory effect observed in the MEC diminished after the blockade of Hcrt type 1 receptor antagonist (Figure S12I), supporting that the LH_{Hcrt}-MEC pathway only releases Hcrt. Additionally, stimulation of the Hcrt fiber-induced excitatory effects was blocked by ionic glutamatergic receptor antagonists (Figure 4L). Stimulation of the Hcrt fibers increased the frequency, but not the amplitude, of excitatory postsynaptic currents in the fast-spiking PV^+ neurons (Figure 4M). Taken together, these results demonstrate that endogenous Hcrt excites fast-spiking PV^+ neurons via stimulation of presynaptic Glu release.

The tight control exerted by glutamatergic neurons over the fast-spiking PV^+ neurons through local microcircuits in the superficial layers of the MEC[56,58] raised the possibility of Hcrt functioning at the presynaptic terminals from these local glutamatergic neurons. To investigate this, we conducted double patch-clamp recordings to study pairs of neurons with somata located <40 μm apart (Figure 4N). Stimulation parameters were set to induce a train of action potentials in the excitatory cell, and the postsynaptic excitatory currents were recorded in another neuron. Following the criterion from a previous study,[56] only postsynaptic excitatory currents with short latency and signal-to-noise ratio (SNR) higher than 2 were classified as unitary excitatory postsynaptic currents (uEPSCs), indicating direct monosynaptic connections. Although direct connections between pairs of glutamatergic cells were rare (1 out of 80), glutamatergic cells innervated inhibitory GABAergic neurons more frequently (18 of the 97) (Figures S12J and S12K). Remarkably, the application of Hcrt-A significantly increased the amplitude and reliability of the uEPSCs in the pairs of excitatory and fast-spiking PV^+ neurons (Figures 4N and 4O), indicating Hcrt's role in elevating functional connectivity from the local glutamatergic neurons to the PV^+ neurons.

Figure 4. Hcrt stimulates presynaptic terminals of the glutamatergic neurons to excite the fast-spiking PV^+ interneurons of the MEC

(A) Morphological and electrophysiological characteristics of a glutamatergic neuron in the superficial layers of the MEC.

(B) Effects of Hcrt on the membrane potentials of the glutamatergic neurons (paired t test, n = 8 cells, p = 0.38). Data are represented as mean ± SEM.

(C) A representative trace of the SIPSCs before, during, and after the application of Hcrt-A (top). Enlarged view of the traces are indicated by the red arrows in the upper panel (bottom).

(D) Cumulative probability curves for interevent interval (left) and amplitude (right) distribution of SIPSCs before and during Hcrt-A application.

(E) Effects of Hcrt-A on the average frequency (one-way RM ANOVA, n = 7 cells, p < 0.001) (left) and amplitude (one-way RM ANOVA, n= 7 cells, p < 0.05) (right) of the SIPSCs. Data are represented as mean ± SEM.

(F) Electrophysiological characteristics of fast-spiking PV^+ neurons in the superficial layers of the MEC.

(G) Effects of Hcrt-A on the spontaneous firing rates of fast-spiking PV^+ neurons (Wilcoxon signed rank test, n = 14 cells, p < 0.001). Data are represented as mean ± SEM.

(H) Effects of Hcrt-A on the firing rates of fast-spiking PV^+ neurons evoked by injections of inward currents (Scheirer-Ray-Hare test, n = 7 cells for each group, treatment: p < 0.01; current factor: p < 0.001; interaction: p = 0.88). Data are represented as mean ± SEM.

(I) Paradigm for *in vitro* characterization of the functional connection of the LH_{Hcrt}-MEC pathway.

(J) Representative trace of membrane potentials of one PV^+ neuron before, during, and after optical stimulation of Hcrt axons (left). Effects of optical stimulation of the Hcrt axons on the spontaneous firing rates of fast-spiking PV^+ interneurons (right) (Wilcoxon signed rank test, n = 12 cells, p < 0.001). Data are represented as mean ± SEM.

(K) Effects of optical stimulation of Hcrt axons on the firing rates of fast-spiking PV^+ neurons evoked by injections of inward currents (Scheirer-Ray-Hare test, n = 6 cells for each group, treatment: p < 0.01; current factor: p < 0.001; interaction: p = 0.99). Data are represented as mean ± SEM.

(L) Effects of optical stimulation of the Hcrt axons on the firing rates of PV^+ neurons in the presence of the α-amino-3-hydroxy-5-methyl-4-isoxazole propionic acid (AMPA) and N-methyl-D-aspartate (NMDA) receptor antagonist 2-amino-5-phosphonovaleric acid (AP5) and 6-Cyano-7-nitroquinoxaline-2,3-dione (CNQX) (Wilcoxon signed rank test, n = 5 cells, p = 0.25). Data are represented as mean ± SEM.

(M) Representative traces of SEPSCs before, during, and after optical stimulation of the Hcrt axons (left). Effects of the optical stimulation of the Hcrt axons on the frequency (Wilcoxon signed rank test, n = 6 cells, p < 0.05) (middle) and amplitude (paired t test, n = 6 cells, p = 0.36) (right) of SEPSCs. Data are represented as mean ± SEM.

(N) Schematic of the apparatus for double patch-clamp recordings of local glutamatergic and PV^+ neurons in the MEC (left). The recorded uEPSCs from glutamatergic neurons to PV^+ neurons before and during application of the Hcrt-A (right).

(O) Reliability (one-way RM ANOVA, n = 5 pairs of cells, p < 0.05) and amplitude (one-way RM ANOVA, n = 5 pairs of cells, p < 0.05) of uEPSCs before and during application of Hcrt-A. Data are represented as mean ± SEM.

(P) Immunoelectron microscopic image showing Hcrt 1 receptors-positive terminal (t) contact with GABAergic neuronal soma. Arrows indicate the Hcrt 1 receptor immunograins. Stars indicate the GABA-immunopositive peroxidase reaction products. Inset shows another Hcrt 1 receptors-positive terminal contact with GABAergic neuronal soma (four independent experiments from 4 mice). n, nucleus.

(Q) Representative images showing contact (indicated by white arrowheads) between the $Hcrt^+$ varicosities and the $EGFP^+$ presynaptic terminals of the glutamatergic neurons. 60% ± 4% (n = 8 brain slices from 4 mice) of the $Hcrt^+$ varicosities are in contact with the presynaptic terminals of the glutamatergic neurons.

(R) Schematic showing the mechanism underlying the Hcrt regulation of PV^+ neurons. Hcrt stimulates the glutamatergic terminals to excite PV^+ neurons in the MEC. See Table S1 for full results of statistical tests.

(legend on next page)

Neuron
Article

CellPress
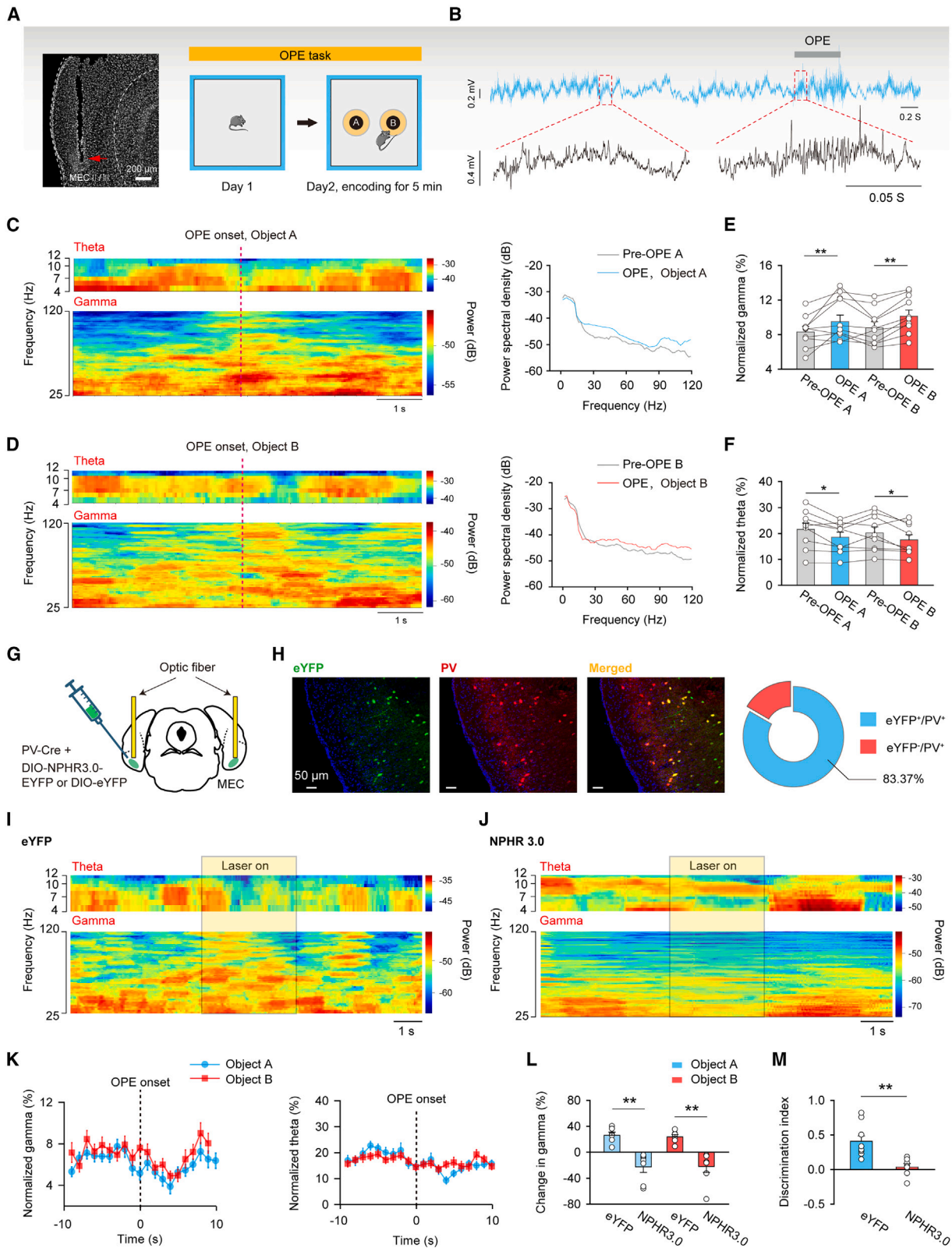
To investigate the subcellular distribution of Hcrt 1 receptors, we employed double-labeling immunohistochemical electron microscopy. Morphological results showed that Hcrt 1 receptors were expressed at the presynaptic excitatory terminals around the somata of the GABAergic neurons (Figure 4P). Furthermore, by labeling the presynaptic terminals of glutamatergic cells using AAV2/9-CaMKIIα-CRE and AAV2/9-hSyn-DIO-Synaptophysin-EGFP in the MEC, combined with immunohistochemical staining for Hcrt-A-positive varicosities, we observed that approximately 60% of Hcrt$^+$ varicosities were in close proximity to the EGFP$^+$ presynaptic terminals of glutamatergic neurons (Figure 4Q). The combined morphological and electrophysiological findings imply that Hcrt stimulates synaptic terminals from excitatory neurons to excite fast-spiking PV$^+$ neurons (Figure 4R).

Next, we compared the effects of the Hcrt system with other wakefulness-promoting systems, including noradrenergic, dopaminergic, serotonergic, and acetylcholinergic systems in the MEC. Noradrenaline had a direct excitatory effect on both glutamatergic and fast-spiking PV$^+$ neurons, without affecting excitatory inputs on fast-spiking PV$^+$ neurons. Dopamine (DA) directly inhibited glutamatergic neurons and enhanced excitatory inputs on fast-spiking PV$^+$ neurons. Serotonin (5-TH) directly inhibited glutamatergic neurons but excited fast-spiking PV$^+$ neurons. Acetylcholine (ACh) only directly excited PV$^+$ neurons in the MEC (Figure S13). These results highlight the unique and distinct feature of Hcrt in selectively stimulating glutamatergic synaptic terminals to activate fast-spiking PV$^+$ neurons, unlike other wakefulness-promoting systems.

MEC gamma oscillations driven by PV$^+$ neurons correlated with spatial memory encoding

Previous studies have demonstrated that fast-spiking PV$^+$ neurons are crucial for generating gamma oscillations *in vivo*.[39–41] Given that Hcrt excites PV$^+$ neurons by stimulating presynaptic glutamatergic terminals in the MEC, we investigated whether PV$^+$ neurons also drive gamma oscillations in the MEC and their involvement in object-place memory encoding. Local field potentials (LFPs) were recorded from the MEC during the object-place memory task (Figures 5A, S14A, and S14B). Compared with the baseline, significant shifts in LFP power occurred during object-place exploration, resulting in synchronized oscillations in the gamma (25–120 Hz) band, but not the theta (4–12 Hz) band (Figures 5B–5F). These findings align with previous reports correlating elevated gamma oscillations with spatial memory encoding in the MEC.[39]

To explore the possible correlation between gamma oscillations driven by fast-spiking PV$^+$ neurons and object-place memory encoding, we performed optogenetic manipulations by expressing either NpHR or eYFP alone in the PV$^+$ neurons of the MEC (Figures 5G, S14C, and S14D). Specificity of NpHR expression in the PV$^+$ neurons was confirmed by immunochemical staining (Figure 5H). During the memory encoding session, mouse exploration within a marked subarea around the objects triggered the delivery of yellow light to inhibit the PV$^+$ neurons. Under this condition, a significant increase in gamma oscillation power was observed in control mice during their approach to the area around object A or object B. However, mice with PV$^+$ neuron inhibition showed a significant decrease in gamma oscillations when approaching the area around both object A and object B (Figures 5I–5L, S14E, and S14F). During the recall stage, mice with optogenetic inhibition of PV$^+$ neurons during encoding were unable to recognize the changed spatial position, displaying a decrease in the discrimination index (Figure 5M). These results suggest that PV$^+$-neuron-driven gamma oscillations are associated with object-place memory encoding.

LH$_{Hcrt}$-MEC pathway supports spatial memory by tuning gamma oscillations and elevating SNRs

After establishing the correlation between gamma oscillations and object-place memory encoding, we investigated whether the LH$_{Hcrt}$-MEC pathway supports object-place memory by influencing gamma oscillations. Using a chemogenetic approach combined with multi-channel single-unit recordings, we selectively inhibited the LH$_{Hcrt}$-MEC pathway (Figure 6A). Consistent with our earlier findings, chemogenetic inhibition during encoding

Figure 5. Gamma oscillations driven by PV$^+$ neurons in the MEC are associated with object-place memory encoding

(A) An image showing the electrode planted in the MEC (left). Red arrow indicates the recording position. Schematic showing the design of the object-place memory task (right).

(B) Examples of the raw electrophysiological traces recorded in the MEC before and during object-place exploration.

(C and D) Spectrogram of the theta and gamma oscillations recorded in the example trials before and during exploring the locations of object A (C) and object B (D) (left). Traces of power spectral density of the local field potential recorded in one example trial before and during exploring locations of object A (C) and object B (D) (right).

(E) Changes in the gamma oscillation power around object-place exploration (one-way RM ANOVA, n = 9 mice, p < 0.001). Data are represented as mean ± SEM.

(F) Changes in the theta oscillation power around object-place exploration (one-way RM ANOVA, n = 9 mice, p < 0.01). Data are represented as mean ± SEM.

(G) Schematic of the optogenetic inhibition of the PV$^+$ neurons when the animals explored the locations of the objects.

(H) An image showing NpHR (green) and immunohistochemical staining for PV (red) in the MEC (left). Quantification of the specificity of Cre-inducible NpHR expression in the MEC of PV-Cre mice (right).

(I and J) Power spectrum of the theta and gamma oscillations recorded in the example trials before, during, and after light stimulation in the eYFP (I) and NpHR (J) groups at the encoding stage.

(K) Line plots showing the changes in the theta and gamma oscillation power around object-place exploration in the NpHR group.

(L) Bar graphs with overlaid dot plots showing the changes in gamma oscillation power around object-place exploration (object A: Mann-Whitney rank sum test, eYFP: n = 6 mice, NpHR: n = 7 mice, p < 0.01; object B: Mann-Whitney rank sum test, eYFP: n = 6 mice, NpHR: n = 7 mice, p < 0.01). Data are represented as mean ± SEM.

(M) Bar graphs with overlaid dot plots showing the changes in discrimination index between the eYFP and NpHR groups (unpaired t test, eYFP: n = 9 mice; NpHR: n = 7 mice, p < 0.01). One mouse was excluded for incorrect location of optical fibers and one mouse was excluded for lack of exploratory motivation. Data are represented as mean ± SEM.

See Table S1 for full results of statistical tests.

Neuron
Article

CellPress
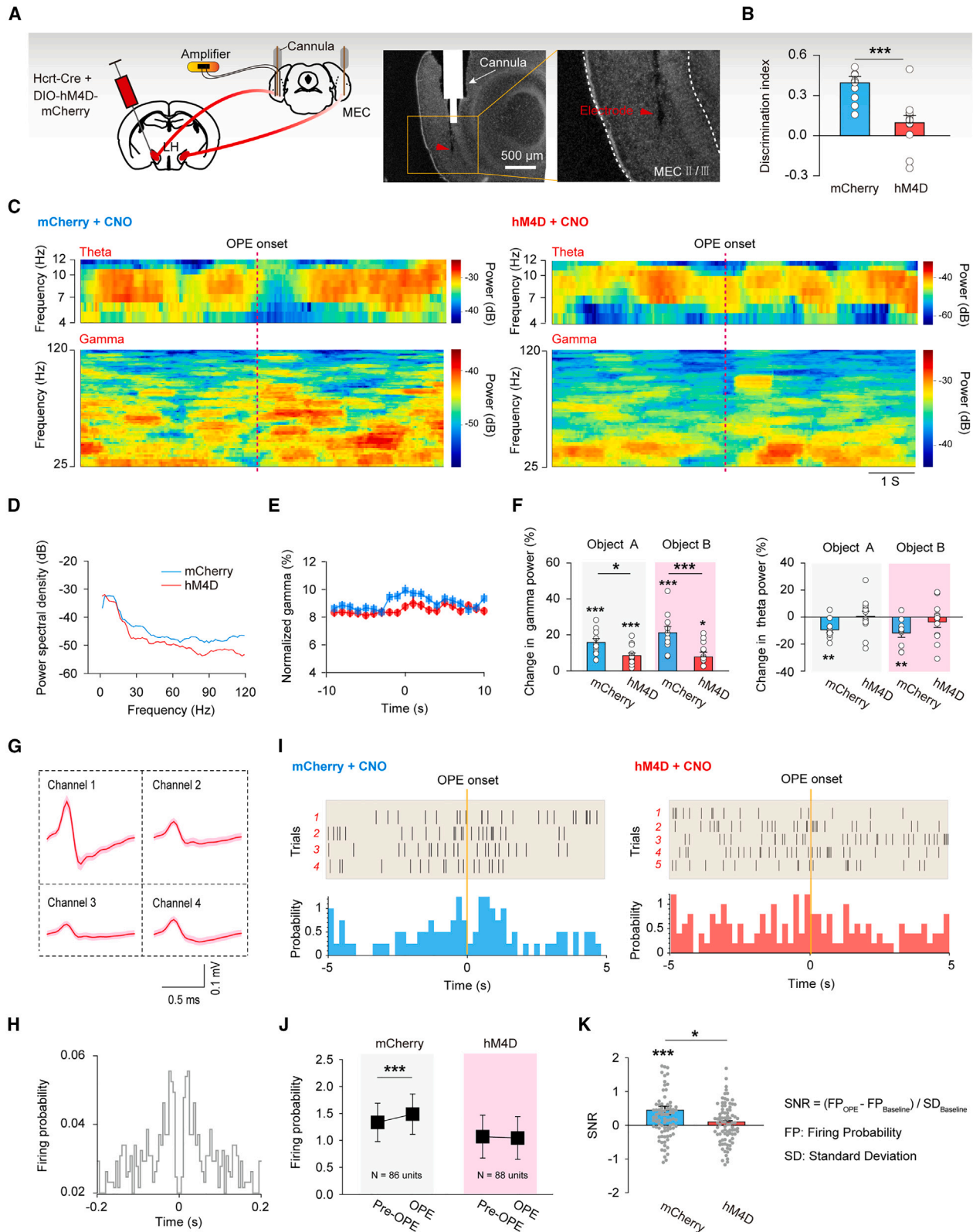
resulted in a decrease in the discrimination index (Figure 6B), indicating impaired object-place memory. Moreover, we examined the increases in MEC gamma power induced by object-place exploration. Although control mice showed significant increases in MEC gamma power during object-place exploration, the magnitude of this increase was significantly attenuated by inhibition of the LH_{Hcrt}-MEC pathway (Figures 6C–6F), suggesting the contribution of LH_{Hcrt}-MEC projections to object-place memory through promoting gamma synchrony.

Recent research has indicated that gamma oscillations in the CA1 of the hippocampus can enhance the SNR of neuronal encoding of object location.[59] Therefore, we investigated whether LH_{Hcrt}-MEC projections affect the encoding properties of entorhinal neurons (Figures 6G and 6H). SNR for each neuron was defined as the change in its firing activity before and during object-place exploration within a zone surrounding the object. Neurons with increased or decreased firing rates in the object zone by one standard deviation had SNR greater or less than zero, respectively. In control mice expressing mCherry, the activity of neurons increased within the object zone, and the average SNR was greater than zero. However, chemogenetic inhibition of the LH_{Hcrt}-MEC pathway abolished the difference in firing rates before and during object-place exploration, significantly decreasing SNR values relative to the control condition (Figures 6I–6K). Together, these results demonstrate that the LH_{Hcrt}-MEC pathway elevates the SNR of neuronal encoding for object-place memory.

DISCUSSION

Our study sheds light on the activation of Hcrt neurons during novel object-place exploration and their significant impact on the spatial memory-associated MEC in the MEC-hippocampal circuit. Using $GRAB_{Hcrt0.5}$ sensors, we observed a notable elevation of Hcrt levels during novel object-place exploration, suggesting that Hcrt neurons play a specific role in spatial memory rather than promoting general arousal. The increased Hcrt neuropeptide stimulates PV^+ neurons by acting on the presynaptic terminals of glutamatergic neurons, thereby enhancing gamma oscillations to support object-place memory encoding. These findings emphasize that spatial memory relies not only on the MEC-hippocampal circuit itself but also on the support provided by the Hcrt systems. As we performed some experiments, such as retrograde tracing, fiber photometry, multi-channel single-unit recording, and behavioral tests, only in male mice, future investigations are needed to validate these findings in female mice.

As of now, the spatiotemporal dynamics of Hcrt release during various behaviors, especially memory-related tasks, remain poorly understood, primarily due to limitations in existing detection methods. However, the development of genetically encoded GRAB sensors has provided an avenue to detect various neurotransmitters and neuromodulators with high sensitivity, selectivity, and spatiotemporal resolution.[44–49] Leveraging our strategy for accelerating the development of a wide variety of GRAB peptide sensors for neuropeptides,[50] we further optimized a genetically encoded $GRAB_{Hcrt0.5}$ sensor with nanomolar affinity and high specificity for detecting endogenous Hcrt release. Compared with another Hcrt sensor, OxLight1,[51] $GRAB_{Hcrt0.5}$ exhibits larger maximum brightness, potentially leading to a better SNR for *in vivo* Hcrt detection. This new sensor enriches our capability to detect neuropeptides, such as Hcrt, enhancing our understanding of their functions.

The entorhinal cortex serves as a crucial gateway structure for the hippocampus and exhibits prominent theta and gamma oscillations during active wakefulness.[2,38,60] Gamma oscillations are known to transiently link distributed neuron assemblies, elevating the SNR of neuronal encoding and playing a critical role in spatial memory.[2,39,59,61] Previous studies have established that increased synchrony of fast-spiking PV^+ neuron activity drives gamma oscillations in several cortical areas and the hippocampus.[41,62–64] Interestingly, selective activation of fast-spiking PV^+ cells induces gamma rhythm, and impairment of these neurons disrupts gamma rhythms and affects cognitive function.[41,63,64] In this context, our findings showing Hcrt's involvement in increasing PV^+ neuron activity and enhancing gamma oscillations during object-place exploration indicate that the Hcrt system provides a substantial driving force for entorhinal gamma oscillations during memory encoding.

Figure 6. LH_{Hcrt}-MEC pathway elevates gamma oscillations and SNRs supporting object-place memory encoding

(A) Schematic of chemogenetic inhibition of Hcrt neurons together with MEC local field potential and single-unit recordings (left). An image showing the electrode and cannula implanted in the MEC (right).

(B) Bar graphs with overlaid dot plots showing the changes in discrimination index between the mCherry and hM4D groups after CNO injection in the MEC (unpaired t test, mCherry: n = 10 mice, hM4D: n = 12 mice, p < 0.001). Data are represented as mean ± SEM.

(C) Spectrogram of the theta and gamma oscillations before and during object-place exploration recorded in one trial in the mCherry (left) and hM4D (right) groups after CNO injection in the MEC.

(D) Traces of power spectral density of the local field potential in the mCherry and hM4D groups after CNO injection during object-place exploration.

(E) Changes in gamma oscillation power around object-place exploration in the mCherry and hM4D groups after CNO injection in the MEC.

(F) Bar graphs with overlaid dot plots showing the changes in the power of gamma oscillations (one-way ANOVA, mCherry: n = 10 mice, hM4D: n = 12 mice, p < 0.01) (left), and theta oscillations (one-way ANOVA, mCherry: n = 10 mice, hM4D: n = 12 mice, p = 0.08) (right) around object-place exploration in the mCherry and hM4D groups after CNO injection in the MEC. Data are represented as mean ± SEM.

(G and H) Representative waveforms (G) and the corresponding autocorrelogram (H) of one spike recorded from the MEC.

(I) Recorded spikes around object-place exploration in the mCherry (left) and hM4D (right) groups after CNO injection in the MEC.

(J) Changes in firing frequency around the object-place exploration in mCherry and hM4D groups after CNO injection in the MEC (mCherry: Wilcoxon signed rank test, n = 86 cells, p < 0.001; hM4D: Wilcoxon signed rank test, n = 88 cells, p = 0.87). Data are represented as mean ± SEM.

(K) Bar graphs with overlayed dot plots showing the alterations in SNR in the mCherry and hM4D groups after CNO injection in the MEC (Mann-Whitney rank sum test, mCherry: n = 86 cells, hM4D: n = 88 cells, p < 0.05; mCherry: one-sample signed rank test, p < 0.001; hM4D: one-sample signed rank test, p = 0.32). Data are represented as mean ± SEM.

See Table S1 for full results of statistical tests.

CellPress

Neuron
Article

Another prominent network activity in the MEC is theta oscillations, representing an online state of the MEC-hippocampal circuit and playing a role in spatial memory.[2,3] Prior studies have highlighted the medial septum/diagonal band as the primary driving force for theta oscillations in the MEC, as inactivation of this area nearly abolishes theta oscillations.[65] These findings suggest that spatial memory task-related theta and gamma network activities might require multiple regulatory systems. It should be noted that previous studies have shown a clear peak within the theta range in the power spectral density analyses,[66,67] which seems to be inconsistent with our findings. The reason for this difference might be variable analysis methods and behavioral paradigms, as the power spectrum was calculated only when the mice were in an exploratory movement state in these previous studies.

Regarding the modulation of GABAergic inhibitory neurons by Hcrt, previous studies have reported that Hcrt regulates these neurons mainly by directly influencing their membrane properties.[68–71] Although there are limited *in vitro* studies showing an indirect excitatory effect of Hcrt on fast-spiking interneurons in the prefrontal cortex,[72] the precise mechanisms are still not well understood. Our study reveals prominent connections from excitatory glutamatergic to inhibitory neurons in the MEC. Hcrt stimulates the presynaptic excitatory terminals mainly from this local microcircuit, enhancing functional connectivity from excitatory to PV$^+$ cells and thereby indirectly synchronizing the activities of PV$^+$ neurons. In contrast, other monoaminergic and cholinergic wakefulness-promoting systems in the MEC either directly affect the activities of excitatory neurons or inhibitory neurons without specific regulation of functional connectivity between these two types of neurons. Thus, our findings unveil a specific integrated microcircuit mechanism neuromodulatory effect of Hcrt system. It should be noted that stimulating Hcrt fibers only mildly increased the frequency, but not the amplitude, of excitatory postsynaptic currents. This moderate effect may be due to the fact that Hcrt is released from varicosity and spreads to postsynaptic cells over a relatively long distance compared with classical chemical synaptic transmissions. Under this condition, perfusion of artificial cerebrospinal fluid *in vitro* can dilute the endogenous release of Hcrt and therefore elicit a moderate effect.

For stable memory engrams to form, neural circuits engaged in encoding and storing memory information must be tightly controlled. Disruptions in synchronization or changes in the number of neurons recruited in these circuits could lead to unstable memory.[73,74] Wakefulness-promoting systems, including cholinergic and monoaminergic systems, have been shown to target different nodes of the entorhinal cortex-hippocampal circuit, supporting specific molecular and cellular events in the memory trace to ensure stable memory formation.[4–6,8,9,75–78] For example, DA signals from the locus coeruleus, ventral tegmental area, and substantia nigra mediate novelty-induced memory enhancement and association memory encoding by controlling the activities of CA1 and lateral entorhinal cortex, respectively.[9,76] Similarly, serotonin from the dorsal raphe modulates social memory via the medial septum-CA2 pathway, whereas serotonin-mediated inhibition of the ventral hippocampus is essential for goal-directed behavior.[77,79] Furthermore, a

locus coeruleus-dorsal CA1 dopaminergic circuit specifically modulates memory linking without affecting memory formation.[5] Our study demonstrates that object-place memory requires the Hcrt system to synchronize distributed neuron assemblies in the gamma-frequency band in the MEC. These findings reinforce the notion that wakefulness-promoting systems act as conductors, orchestrating neuronal activities in memory traces and enabling highly efficient memory encoding during wakefulness. This principle may explain why memory-related circuits are innervated by multiple wakefulness-promoting systems and serve as the basis for a theoretical framework that unifies the roles of two central components of spatial memory: neuromodulatory systems and the MEC-hippocampal circuit.

It should be noted that MEC contains many types of functional cells, such as grid cells, head direction cells, and even the recently discovered speed cells, and is also involved in contextual memory and spatial navigation.[1,3,80–82] This study mainly focused on object-place memory and the related neural network oscillations. However, it remains unclear whether and how Hcrt system modulates these functional cell activities and other MEC-related behaviors. The fact that the Hcrt system is activated to some extent during the exploration of a novel environment, although to a lesser extent than during object-place exploration, suggests its potential involvement in contextual memory formation. Furthermore, Hcrt neurons have abundant projections to the MEC, but these neurons also have moderate projections to the lateral entorhinal cortex among adjacent regions. Considering that lateral entorhinal cortex is involved in novel object recognition,[4,39] Hcrt system might have some other additional functions.

STAR★METHODS

Detailed methods are provided in the online version of this paper and include the following:

- KEY RESOURCES TABLE
- RESOURCE AVAILABILITY
  - ○ Lead contact
  - ○ Materials availability
  - ○ Data and code availability
- EXPERIMENTAL MODEL AND STUDY PARTICIPANT DETAILS
- METHOD DETAILS
  - ○ Stereotactic injections and cannula implantation
  - ○ Retrograde and anterograde tracing
  - ○ Behavioral tests
  - ○ Closed-loop optogenetic intervention
  - ○ Development and characterization of the GRAB$_{Hcrt0.5}$ sensor
  - ○ *In vivo* fiber photometry
  - ○ Multi-channel single-unit recording
  - ○ Whole-cell patch clamp recordings
  - ○ Intraperitoneal injection and cannula infusion of drugs
  - ○ Immunohistochemistry
  - ○ Immune electron microscopy
  - ○ Histological identification
- QUANTIFICATION AND STATISTICAL ANALYSIS

Neuron
Article

CellPress

AUTHOR CONTRIBUTIONS

Z.H., C.H., J.X. Xia., S.W., X.C., and Y. Li designed the experiments. Y. Liao, R.W., S.F., X. Cheng, S.R., M.L., L.Q., F.L., Yaling Wang, Q.X., X.W., H.Y., X.Z., X.L., S.L., R.D., Y. Liu, J.K., J.Y., and C.H. executed the experiments and conducted statistical analysis. Y. Liao, R.W., Z.H., and C.H. wrote the paper with the help of C.J., Z.Y., J.X. Xiong., Yanjiang Wang, S.W., X.C., and Y. Li. All authors read and commented on the manuscript. Z.H., C.H., and J.X. Xia. supervised the study. Z.H., C.H., and J.Y. obtained funding.

DECLARATION OF INTERESTS

The authors declare no competing interests.

REFERENCES

1. Buzsáki, G., and Llinás, R. (2017). Space and time in the brain. Science 358, 482–485. https://doi.org/10.1126/science.aan8869.

2. Colgin, L.L. (2016). Rhythms of the hippocampal network. Nat. Rev. Neurosci. 17, 239–249. https://doi.org/10.1038/nrn.2016.21.

3. Buzsáki, G., and Moser, E.I. (2013). Memory, navigation and theta rhythm in the hippocampal-entorhinal system. Nat. Neurosci. 16, 130–138. https://doi.org/10.1038/nn.3304.

4. Chen, Q., Luo, F., Yue, F., Xia, J., Xiao, Q., Liao, X., Jiang, J., Zhang, J., Hu, B., Gao, D., et al. (2018). Histamine enhances theta-coupled spiking and gamma oscillations in the medial entorhinal cortex consistent with successful spatial recognition. Cereb. Cortex 28, 2439–2457. https://doi.org/10.1093/cercor/bhx145.

5. Chowdhury, A., Luchetti, A., Fernandes, G., Filho, D.A., Kastellakis, G., Tzilivaki, A., Ramirez, E.M., Tran, M.Y., Poirazi, P., and Silva, A.J. (2022). A locus coeruleus-dorsal CA1 dopaminergic circuit modulates memory linking. Neuron 110, 3374–3388.e8. https://doi.org/10.1016/j.neuron.2022.08.001.

6. Hasselmo, M.E. (2006). The role of acetylcholine in learning and memory. Curr. Opin. Neurobiol. 16, 710–715. https://doi.org/10.1016/j.conb.2006.09.002.

7. He, C., Luo, F., Chen, X., Chen, F., Li, C., Ren, S., Qiao, Q., Zhang, J., de Lecea, L., Gao, D., and Hu, Z. (2016). Superficial layer-specific histaminergic modulation of medial entorhinal cortex required for spatial learning. Cereb. Cortex 26, 1590–1608. https://doi.org/10.1093/cercor/bhu322.

8. Li, Y., Bao, H., Luo, Y., Yoan, C., Sullivan, H.A., Quintanilla, L., Wickersham, I., Lazarus, M., Shih, Y.I., and Song, J. (2020). Supramammillary nucleus synchronizes with dentate gyrus to regulate spatial memory retrieval through glutamate release. eLife 9, e53129. https://doi.org/10.7554/eLife.53129.

9. Takeuchi, T., Duszkiewicz, A.J., Sonneborn, A., Spooner, P.A., Yamasaki, M., Watanabe, M., Smith, C.C., Fernández, G., Deisseroth, K., Greene, R.W., and Morris, R.G. (2016). Locus coeruleus and dopaminergic consolidation of everyday memory. Nature 537, 357–362. https://doi.org/10.1038/nature19325.

10. Liu, D., and Dan, Y. (2019). A motor theory of sleep-wake control: arousal-action circuit. Annu. Rev. Neurosci. 42, 27–46. https://doi.org/10.1146/annurev-neuro-080317-061813.

11. Weber, F., and Dan, Y. (2016). Circuit-based interrogation of sleep control. Nature 538, 51–59. https://doi.org/10.1038/nature19773.

12. Newman, E.L., Venditto, S.J.C., Climer, J.R., Petter, E.A., Gillet, S.N., and Levy, S. (2017). Precise spike timing dynamics of hippocampal place cell activity sensitive to cholinergic disruption. Hippocampus 27, 1069–1082. https://doi.org/10.1002/hipo.22753.

13. Benussi, A., Cantoni, V., Grassi, M., Brechet, L., Michel, C.M., Datta, A., Thomas, C., Gazzina, S., Cotelli, M.S., Bianchi, M., et al. (2022). Increasing brain gamma activity improves episodic memory and restores cholinergic dysfunction in Alzheimer's disease. Ann. Neurol. 92, 322–334. https://doi.org/10.1002/ana.26411.

14. Bostancıklıoğlu, M. (2020). Optogenetic stimulation of serotonin nuclei retrieve the lost memory in Alzheimer's disease. J. Cell. Physiol. 235, 836–847. https://doi.org/10.1002/jcp.29077.

15. Burjanadze, M.A., Dashniani, M.G., Solomonia, R.O., Beselia, G.V., Tsverava, L., Lagani, V., Chkhikvishvili, N.C., Naneishvili, T.L., Kruashvili, L.B., and Chighladze, M.R. (2022). Age-related changes in medial septal cholinergic and GABAergic projection neurons and hippocampal neurotransmitter receptors: relationship with memory impairment. Exp. Brain Res. 240, 1589–1604. https://doi.org/10.1007/s00221-022-06354-2.

16. Coray, R., and Quednow, B.B. (2022). The role of serotonin in declarative memory: A systematic review of animal and human research. Neurosci. Biobehav. Rev. 139, 104729. https://doi.org/10.1016/j.neubiorev.2022.104729.

17. Kourosh-Arami, M., Komaki, A., and Zarrindast, M.R. (2023). Dopamine as a potential target for learning and memory: contribution to related neurological disorders. CNS Neurol. Disord. Drug Targets 22, 558–576. https://doi.org/10.2174/1871527321666220418115503.

18. Sakurai, T., Amemiya, A., Ishii, M., Matsuzaki, I., Chemelli, R.M., Tanaka, H., Williams, S.C., Richardson, J.A., Kozlowski, G.P., Wilson, S., et al. (1998). Orexins and orexin receptors: a family of hypothalamic neuropeptides and G protein-coupled receptors that regulate feeding behavior. Cell 92, 573–585. https://doi.org/10.1016/S0092-8674(00)80949-6.

19. Hagan, J.J., Leslie, R.A., Patel, S., Evans, M.L., Wattam, T.A., Holmes, S., Benham, C.D., Taylor, S.G., Routledge, C., Hemmati, P., et al. (1999). Orexin A activates locus coeruleus cell firing and increases arousal in the rat. Proc. Natl. Acad. Sci. USA 96, 10911–10916. https://doi.org/10.1073/pnas.96.19.10911.

20. Adamantidis, A.R., Zhang, F., Aravanis, A.M., Deisseroth, K., and de Lecea, L. (2007). Neural substrates of awakening probed with optogenetic control of hypocretin neurons. Nature 450, 420–424. https://doi.org/10.1038/nature06310.

21. Sakurai, T. (2014). The role of orexin in motivated behaviours. Nat. Rev. Neurosci. 15, 719–731. https://doi.org/10.1038/nrn3837.

22. Aitta-aho, T., Pappa, E., Burdakov, D., and Apergis-Schoute, J. (2016). Cellular activation of hypothalamic hypocretin/orexin neurons facilitates short-term spatial memory in mice. Neurobiol. Learn. Mem. 136, 183–188. https://doi.org/10.1016/j.nlm.2016.10.005.

23. Akbari, E., Motamedi, F., Naghdi, N., and Noorbakhshnia, M. (2008). The effect of antagonization of orexin 1 receptors in CA1 and dentate gyrus regions on memory processing in passive avoidance task. Behav. Brain Res. 187, 172–177. https://doi.org/10.1016/j.bbr.2007.09.019.

24. Akbari, E., Naghdi, N., and Motamedi, F. (2007). The selective orexin 1 receptor antagonist SB-334867-A impairs acquisition and consolidation but not retrieval of spatial memory in Morris water maze. Peptides 28, 650–656. https://doi.org/10.1016/j.peptides.2006.11.002.

25. Dang, R., Chen, Q., Song, J., He, C., Zhang, J., Xia, J., and Hu, Z. (2018). Orexin knockout mice exhibit impaired spatial working memory. Neurosci. Lett. *668*, 92–97. https://doi.org/10.1016/j.neulet.2018.01.013.

26. García-Brito, S., Aldavert-Vera, L., Huguet, G., Kádár, E., and Segura-Torres, P. (2020). Orexin-1 receptor blockade differentially affects spatial and visual discrimination memory facilitation by intracranial self-stimulation. Neurobiol. Learn. Mem. *169*, 107188. https://doi.org/10.1016/j.nlm.2020.107188.

27. Jaeger, L.B., Farr, S.A., Banks, W.A., and Morley, J.E. (2002). Effects of orexin-A on memory processing. Peptides *23*, 1683–1688. https://doi.org/10.1016/s0196-9781(02)00110-9.

28. Naumann, A., Bellebaum, C., and Daum, I. (2006). Cognitive deficits in narcolepsy. J. Sleep Res. *15*, 329–338. https://doi.org/10.1111/j.1365-2869.2006.00533.x.

29. Sadeghi, B., Ezzatpanah, S., and Haghparast, A. (2016). Effects of dorsal hippocampal orexin-2 receptor antagonism on the acquisition, expression, and extinction of morphine-induced place preference in rats. Psychopharmacology *233*, 2329–2341. https://doi.org/10.1007/s00213-016-4280-3.

30. Sartor, G.C., and Aston-Jones, G.S. (2012). A septal-hypothalamic pathway drives orexin neurons, which is necessary for conditioned cocaine preference. J. Neurosci. *32*, 4623–4631. https://doi.org/10.1523/JNEUROSCI.4561-11.2012.

31. Telegdy, G., and Adamik, A. (2002). The action of orexin A on passive avoidance learning. Involvement of transmitters. Regul. Pept. *104*, 105–110. https://doi.org/10.1016/s0167-0115(01)00341-x.

32. Yang, L., Zou, B., Xiong, X., Pascual, C., Xie, J., Malik, A., Xie, J., Sakurai, T., and Xie, X.S. (2013). Hypocretin/orexin neurons contribute to hippocampus-dependent social memory and synaptic plasticity in mice. J. Neurosci. *33*, 5275–5284. https://doi.org/10.1523/JNEUROSCI.3200-12.2013.

33. Han, D., Han, F., Shi, Y., Zheng, S., and Wen, L. (2020). Mechanisms of memory impairment induced by orexin-A via orexin 1 and orexin 2 receptors in post-traumatic stress disorder rats. Neuroscience *432*, 126–136. https://doi.org/10.1016/j.neuroscience.2020.02.026.

34. Raoof, R., Esmaeili-Mahani, S., Abbasnejad, M., Raoof, M., Sheibani, V., Kooshki, R., Amirkhosravi, L., and Rafie, F. (2015). Changes in hippocampal orexin 1 receptor expression involved in tooth pain-induced learning and memory impairment in rats. Neuropeptides *50*, 9–16. https://doi.org/10.1016/j.npep.2015.03.002.

35. Shahsavari, F., Abbasnejad, M., Esmaeili-Mahani, S., and Raoof, M. (2018). Orexin-1 receptors in the rostral ventromedial medulla are involved in the modulation of capsaicin evoked pulpal nociception and impairment of learning and memory. Int. Endod. J. *51*, 1398–1409. https://doi.org/10.1111/iej.12958.

36. Stanojlovic, M., Pallais, J.P., Lee, M.K., and Kotz, C.M. (2019). Pharmacological and chemogenetic orexin/hypocretin intervention ameliorates Hipp-dependent memory impairment in the A53T mice model of Parkinson's disease. Mol. Brain *12*, 87. https://doi.org/10.1186/s13041-019-0514-8.

37. Zhao, X., Zhang, R., Tang, S., Ren, Y., Yang, W., Liu, X., and Tang, Jy. (2014). Orexin-A-induced ERK1/2 activation reverses impaired spatial learning and memory in pentylenetetrazol-kindled rats via OX1R-mediated hippocampal neurogenesis. Peptides *54*, 140–147. https://doi.org/10.1016/j.peptides.2013.11.019.

38. Colgin, L.L., Denninger, T., Fyhn, M., Hafting, T., Bonnevie, T., Jensen, O., Moser, M.B., and Moser, E.I. (2009). Frequency of gamma oscillations routes flow of information in the hippocampus. Nature *462*, 353–357. https://doi.org/10.1038/nature08573.

39. Fernández-Ruiz, A., Oliva, A., Soula, M., Rocha-Almeida, F., Nagy, G.A., Martin-Vazquez, G., and Buzsáki, G. (2021). Gamma rhythm communication between entorhinal cortex and dentate gyrus neuronal assemblies. Science *372*, eabf3119. https://doi.org/10.1126/science.abf3119.

40. Buzsáki, G., and Wang, X.J. (2012). Mechanisms of gamma oscillations. Annu. Rev. Neurosci. *35*, 203–225. https://doi.org/10.1146/annurev-neuro-062111-150444.

41. Cardin, J.A., Carlén, M., Meletis, K., Knoblich, U., Zhang, F., Deisseroth, K., Tsai, L.H., and Moore, C.I. (2009). Driving fast-spiking cells induces gamma rhythm and controls sensory responses. Nature *459*, 663–667. https://doi.org/10.1038/nature08002.

42. Kosse, C., and Burdakov, D. (2019). Natural hypothalamic circuit dynamics underlying object memorization. Nat. Commun. *10*, 2505. https://doi.org/10.1038/s41467-019-10484-7.

43. Moser, E.I., Moser, M.B., and McNaughton, B.L. (2017). Spatial representation in the hippocampal formation: a history. Nat. Neurosci. *20*, 1448–1464. https://doi.org/10.1038/nn.4653.

44. Feng, J., Zhang, C., Lischinsky, J.E., Jing, M., Zhou, J., Wang, H., Zhang, Y., Dong, A., Wu, Z., Wu, H., et al. (2019). A genetically encoded fluorescent sensor for rapid and specific in vivo detection of norepinephrine. Neuron *102*, 745–761.e8. https://doi.org/10.1016/j.neuron.2019.02.037.

45. Jing, M., Li, Y., Zeng, J., Huang, P., Skirzewski, M., Kljakic, O., Peng, W., Qian, T., Tan, K., Zou, J., et al. (2020). An optimized acetylcholine sensor for monitoring in vivo cholinergic activity. Nat. Methods *17*, 1139–1146. https://doi.org/10.1038/s41592-020-0953-2.

46. Qian, T., Wang, H., Wang, P., Geng, L., Mei, L., Osakada, T., Wang, L., Tang, Y., Kania, A., Grinevich, V., et al. (2023). A genetically encoded sensor measures temporal oxytocin release from different neuronal compartments. Nat. Biotechnol. *41*, 944–957. https://doi.org/10.1038/s41587-022-01561-2.

47. Sun, F., Zeng, J., Jing, M., Zhou, J., Feng, J., Owen, S.F., Luo, Y., Li, F., Wang, H., Yamaguchi, T., et al. (2018). A genetically encoded fluorescent sensor enables rapid and specific detection of dopamine in flies, fish, and mice. Cell *174*, 481–496.e19. https://doi.org/10.1016/j.cell.2018.06.042.

48. Wan, J., Peng, W., Li, X., Qian, T., Song, K., Zeng, J., Deng, F., Hao, S., Feng, J., Zhang, P., et al. (2021). A genetically encoded sensor for measuring serotonin dynamics. Nat. Neurosci. *24*, 746–752. https://doi.org/10.1038/s41593-021-00823-7.

49. Wu, Z., He, K., Chen, Y., Li, H., Pan, S., Li, B., Liu, T., Xi, F., Deng, F., Wang, H., et al. (2022). A sensitive GRAB sensor for detecting extracellular ATP in vitro and in vivo. Neuron *110*, 770–782.e5. https://doi.org/10.1016/j.neuron.2021.11.027.

50. Huan Wang, T.Q., Zhao, Y., Zhuo, Y., Wu, C., Osakada, T., Chen, P., Ren, H., Yan, Y., Geng, L., Fu, S., et al. (2022). A toolkit of highly selective and sensitive genetically encoded neuropeptide sensors. Preprint at bioRxiv. https://doi.org/10.1101/2022.03.26.485911.

51. Duffet, L., Kosar, S., Panniello, M., Viberti, B., Bracey, E., Zych, A.D., Radoux-Mergault, A., Zhou, X., Dernic, J., Ravotto, L., et al. (2022). A genetically encoded sensor for in vivo imaging of orexin neuropeptides. Nat. Methods *19*, 231–241. https://doi.org/10.1038/s41592-021-01390-2.

52. Gomez, J.L., Bonaventura, J., Lesniak, W., Mathews, W.B., Sysa-Shah, P., Rodriguez, L.A., Ellis, R.J., Richie, C.T., Harvey, B.K., Dannals, R.F., et al. (2017). Chemogenetics revealed: DREADD occupancy and activation via converted clozapine. Science *357*, 503–507. https://doi.org/10.1126/science.aan2475.

53. Ilg, A.K., Enkel, T., Bartsch, D., and Bähner, F. (2018). Behavioral effects of acute systemic low-dose clozapine in wild-type rats: implications for the use of DREADDs in behavioral neuroscience. Front. Behav. Neurosci. *12*, 173. https://doi.org/10.3389/fnbeh.2018.00173.

54. Manvich, D.F., Webster, K.A., Foster, S.L., Farrell, M.S., Ritchie, J.C., Porter, J.H., and Weinshenker, D. (2018). The DREADD agonist clozapine N-oxide (CNO) is reverse-metabolized to clozapine and produces clozapine-like interoceptive stimulus effects in rats and mice. Sci. Rep. *8*, 3840. https://doi.org/10.1038/s41598-018-22116-z.

55. Liu, Z., Zhou, J., Li, Y., Hu, F., Lu, Y., Ma, M., Feng, Q., Zhang, J.E., Wang, D., Zeng, J., et al. (2014). Dorsal raphe neurons signal reward through 5-HT and glutamate. Neuron *81*, 1360–1374. https://doi.org/10.1016/j.neuron.2014.02.010.

56. Fuchs, E.C., Neitz, A., Pinna, R., Melzer, S., Caputi, A., and Monyer, H. (2016). Local and distant input controlling excitation in layer II of the medial

Neuron
Article

🔖 CellPress

entorhinal cortex. Neuron 89, 194–208. https://doi.org/10.1016/j.neuron.2015.11.029.

57. Carter, M.E., Brill, J., Bonnavion, P., Huguenard, J.R., Huerta, R., and de Lecea, L. (2012). Mechanism for hypocretin-mediated sleep-to-wake transitions. Proc. Natl. Acad. Sci. USA 109, E2635–E2644. https://doi.org/10.1073/pnas.1202526109.

58. Schmidt, H., Gour, A., Straehle, J., Boergens, K.M., Brecht, M., and Helmstaedter, M. (2017). Axonal synapse sorting in medial entorhinal cortex. Nature 549, 469–475. https://doi.org/10.1038/nature24005.

59. Malik, R., Li, Y., Schamiloglu, S., and Sohal, V.S. (2022). Top-down control of hippocampal signal-to-noise by prefrontal long-range inhibition. Cell 185, 1602–1617.e17. https://doi.org/10.1016/j.cell.2022.04.001.

60. Dang, R., Zhou, Y., Zhang, Y., Liu, D., Wu, M., Liu, A., Jia, Z., and Xie, W. (2022). Regulation of social memory by lateral entorhinal cortical projection to dorsal hippocampal CA2. Neurosci. Bull. 38, 318–322. https://doi.org/10.1007/s12264-021-00813-6.

61. Yamamoto, J., Suh, J., Takeuchi, D., and Tonegawa, S. (2014). Successful execution of working memory linked to synchronized high-frequency gamma oscillations. Cell 157, 845–857. https://doi.org/10.1016/j.cell.2014.04.009.

62. Tukker, J.J., Fuentealba, P., Hartwich, K., Somogyi, P., and Klausberger, T. (2007). Cell type-specific tuning of hippocampal interneuron firing during gamma oscillations in vivo. J. Neurosci. 27, 8184–8189. https://doi.org/10.1523/JNEUROSCI.1685-07.2007.

63. Cho, K.K., Hoch, R., Lee, A.T., Patel, T., Rubenstein, J.L., and Sohal, V.S. (2015). Gamma rhythms link prefrontal interneuron dysfunction with cognitive inflexibility in Dlx5/6(+/-) mice. Neuron 85, 1332–1343. https://doi.org/10.1016/j.neuron.2015.02.019.

64. Kim, H., Ährlund-Richter, S., Wang, X., Deisseroth, K., and Carlén, M. (2016). Prefrontal parvalbumin neurons in control of attention. Cell 164, 208–218. https://doi.org/10.1016/j.cell.2015.11.038.

65. Brandon, M.P., Bogaard, A.R., Libby, C.P., Connerney, M.A., Gupta, K., and Hasselmo, M.E. (2011). Reduction of theta rhythm dissociates grid cell spatial periodicity from directional tuning. Science 332, 595–599. https://doi.org/10.1126/science.1201652.

66. Lepperød, M.E., Christensen, A.C., Lensjø, K.K., Buccino, A.P., Yu, J., Fyhn, M., and Hafting, T. (2021). Optogenetic pacing of medial septum parvalbumin-positive cells disrupts temporal but not spatial firing in grid cells. Sci. Adv. 7, eabd5684. https://doi.org/10.1126/sciadv.abd5684.

67. Carpenter, F., Burgess, N., and Barry, C. (2017). Modulating medial septal cholinergic activity reduces medial entorhinal theta frequency without affecting speed or grid coding. Sci. Rep. 7, 14573. https://doi.org/10.1038/s41598-017-15100-6.

68. Belle, M.D., Hughes, A.T., Bechtold, D.A., Cunningham, P., Pierucci, M., Burdakov, D., and Piggins, H.D. (2014). Acute suppressive and long-term phase modulation actions of orexin on the mammalian circadian clock. J. Neurosci. 34, 3607–3621. https://doi.org/10.1523/JNEUROSCI.3388-13.2014.

69. Burdakov, D., Liss, B., and Ashcroft, F.M. (2003). Orexin excites GABAergic neurons of the arcuate nucleus by activating the sodium-calcium exchanger. J. Neurosci. 23, 4951–4957.

70. Korotkova, T.M., Eriksson, K.S., Haas, H.L., and Brown, R.E. (2002). Selective excitation of GABAergic neurons in the substantia nigra of the rat by orexin/hypocretin in vitro. Regul. Pept. 104, 83–89. https://doi.org/10.1016/s0167-0115(01)00323-8.

71. Wu, M., Zhang, Z., Leranth, C., Xu, C., van den Pol, A.N., and Alreja, M. (2002). Hypocretin increases impulse flow in the septohippocampal GABAergic pathway: implications for arousal via a mechanism of hippocampal disinhibition. J. Neurosci. 22, 7754–7765.

72. Aracri, P., Banfi, D., Pasini, M.E., Amadeo, A., and Becchetti, A. (2015). Hypocretin (orexin) regulates glutamate input to fast-spiking interneurons in layer V of the Fr2 region of the murine prefrontal cortex. Cereb. Cortex 25, 1330–1347. https://doi.org/10.1093/cercor/bht326.

73. Lovett-Barron, M., Kaifosh, P., Kheirbek, M.A., Danielson, N., Zaremba, J.D., Reardon, T.R., Turi, G.F., Hen, R., Zemelman, B.V., and Losonczy, A. (2014). Dendritic inhibition in the hippocampus supports fear learning. Science 343, 857–863. https://doi.org/10.1126/science.1247485.

74. Szőnyi, A., Sos, K.E., Nyilas, R., Schlingloff, D., Domonkos, A., Takács, V.T., Pósfai, B., Hegedüs, P., Priestley, J.B., Gundlach, A.L., et al. (2019). Brainstem nucleus incertus controls contextual memory formation. Science 364, eaaw0445. https://doi.org/10.1126/science.aaw0445.

75. Adel, M., and Griffith, L.C. (2021). The role of dopamine in associative learning in drosophila: an updated Unified Model. Neurosci. Bull. 37, 831–852. https://doi.org/10.1007/s12264-021-00665-0.

76. Lee, J.Y., Jun, H., Soma, S., Nakazono, T., Shiraiwa, K., Dasgupta, A., Nakagawa, T., Xie, J.L., Chavez, J., Romo, R., et al. (2021). Dopamine facilitates associative memory encoding in the entorhinal cortex. Nature 598, 321–326. https://doi.org/10.1038/s41586-021-03948-8.

77. Wu, X., Morishita, W., Beier, K.T., Heifets, B.D., and Malenka, R.C. (2021). 5-HT modulation of a medial septal circuit tunes social memory stability. Nature 599, 96–101. https://doi.org/10.1038/s41586-021-03956-8.

78. Yoder, R.M., and Pang, K.C. (2005). Involvement of GABAergic and cholinergic medial septal neurons in hippocampal theta rhythm. Hippocampus 15, 381–392. https://doi.org/10.1002/hipo.20062.

79. Yoshida, K., Drew, M.R., Mimura, M., and Tanaka, K.F. (2019). Serotonin-mediated inhibition of ventral hippocampus is required for sustained goal-directed behavior. Nat. Neurosci. 22, 770–777. https://doi.org/10.1038/s41593-019-0376-5.

80. Schmidt-Hieber, C., and Häusser, M. (2013). Cellular mechanisms of spatial navigation in the medial entorhinal cortex. Nat. Neurosci. 16, 325–331. https://doi.org/10.1038/nn.3340.

81. Kitamura, T., Pignatelli, M., Suh, J., Kohara, K., Yoshiki, A., Abe, K., and Tonegawa, S. (2014). Island cells control temporal association memory. Science 343, 896–901. https://doi.org/10.1126/science.1244634.

82. Suh, J., Rivest, A.J., Nakashiba, T., Tominaga, T., and Tonegawa, S. (2011). Entorhinal cortex layer III input to the hippocampus is crucial for temporal association memory. Science 334, 1415–1420. https://doi.org/10.1126/science.1210125.

83. Sawangjit, A., Oyanedel, C.N., Niethard, N., Salazar, C., Born, J., and Inostroza, M. (2018). The hippocampus is crucial for forming non-hippocampal long-term memory during sleep. Nature 564, 109–113. https://doi.org/10.1038/s41586-018-0716-8.

84. Bilsland, J.G., Wheeldon, A., Mead, A., Znamenskiy, P., Almond, S., Waters, K.A., Thakur, M., Beaumont, V., Bonnert, T.P., Heavens, R., et al. (2008). Behavioral and neurochemical alterations in mice deficient in anaplastic lymphoma kinase suggest therapeutic potential for psychiatric indications. Neuropsychopharmacology 33, 685–700. https://doi.org/10.1038/sj.npp.1301446.

85. Clarke, J.R., Cammarota, M., Gruart, A., Izquierdo, I., and Delgado-García, J.M. (2010). Plastic modifications induced by object recognition memory processing. Proc. Natl. Acad. Sci. USA 107, 2652–2657. https://doi.org/10.1073/pnas.0915059107.

86. Ennaceur, A., and Delacour, J. (1988). A new one-trial test for neurobiological studies of memory in rats. 1: Behavioral data. Behav. Brain Res. 31, 47–59. https://doi.org/10.1016/0166-4328(88)90157-x.

87. Li, Y., Fan, S., Yan, J., Li, B., Chen, F., Xia, J., Yu, Z., and Hu, Z. (2011). Adenosine modulates the excitability of layer II stellate neurons in entorhinal cortex through A1 receptors. Hippocampus 21, 265–280. https://doi.org/10.1002/hipo.20745.

88. Deng, P.-Y., and Lei, S. (2008). Serotonin increases GABA release in rat entorhinal cortex by inhibiting interneuron TASK-3 K⁺ channels. Mol. Cell. Neurosci. 39, 273–284. https://doi.org/10.1016/j.mcn.2008.07.005.

STAR★METHODS

KEY RESOURCES TABLE

REAGENT or RESOURCE	SOURCE	IDENTIFIER
Antibodies		
Goat polyclonal anti-HcrtR1	Origene	CAT#TA303362
Goat polyclonal anti-Hcrt-A	Santa Cruz	CAT#SC-8070
Rabbit polyclonal anti-GABA	Sigma-Aldrich	CAT# A2052
Rabbit polyclonal anti-c-Fos	Millipore	CAT#ABE457
Alexa Flour 488 donkey Anti-rabbit	Invitrogen	CAT#A32790; RRID: AB_2762833
Alexa Flour 568 donkey Anti-goat	Invitrogen	CAT#A-11057; RRID: AB_2534104
Alexa Flour 488 donkey Anti-goat	Invitrogen	CAT#A32814; RRID: AB_2762838
Alexa Flour 647 donkey Anti-goat	Invitrogen	CAT#A32849; RRID: AB_2762840
Bacterial and virus strains		
rAAV2/9-EF1α-DIO-ChR2-mCherry	Obio Technology Co. Ltd.	N/A
rAAV2/9-EF1α-DIO-NpHR3.0-eYFP	BrainVTA Technology Co. Ltd.	N/A
rAAV2/9-EF1α-DIO-mCherry	BrainCase Technology Co. Ltd.	N/A
rAAV2/9-EF1α-DIO-eYFP	BrainVTA Technology Co. Ltd.	N/A
rAAV2/9-EF1α-DIO-hM3D-mCherry	BrainVTA Technology Co. Ltd.	N/A
rAAV2/9-EF1α-DIO-hM4D-mCherry	BrainVTA Technology Co. Ltd.	N/A
rAAV2/9-EF1α-DIO-GCaMP6f	Obio Technology Co. Ltd.	N/A
rAAV2/9-CaMKIIα-CRE	BrainVTA Technology Co. Ltd.	N/A
rAAV2/9-hSyn-DIO-Synaptophysin-EGFP	BrainVTA Technology Co. Ltd.	N/A
Chemicals, peptides, and recombinant proteins		
Clozapine N-oxide	Tocris	CAT#4936
Red retrobeads	Lumafluor	CAT#78R180
Hcrt-A	Tocris	CAT#1455
SB-334867	Tocris	CAT#1960
CNQX	Tocris	CAT#0190
AP-5	Tocris	CAT#0105
Na2-GTP	Sigma-Aldrich	CAT#51120
Na2-ATP	Sigma-Aldrich	CAT#A26209
HEPES	Sigma-Aldrich	CAT#RDD002
PIC	Tocris	CAT#1128
Suvorexant	Abmole	CAT#M2272
EGTA	Sigma-Aldrich	CAT#E3889
Experimental models: Organisms/strains		
Hcrt-Cre mice	Luis de Lecea Lab	N/A
GAD67-GFP mice	The Jackson Laboratory	Stock #007677
PV-Cre mice	The Jackson Laboratory	Stock #008069
Software and algorithms		
MATLAB	Mathworks	https://www.mathworks.com/
NeuroExplorer	Nex Technologies	https://www.neuroexplorer.com/
Igor Pro	WaveMetrics	https://www.wavemetrics.com/
Patchmaster	HEKA Elektronik	http://www.heka.com/index.html
MiniAnalysis	Synaptosoft Inc.	https://en.freedownloadmanager.org/Windows-PC/Mini-Analysis-Program.html
Cheetah	Neuralynx Inc.	https://neuralynx.com/
SpikeSort3D	Neuralynx Inc.	https://neuralynx.com/

Neuron
Article

CellPress

RESOURCE AVAILABILITY

Lead contact
Further information and requests for resources and reagents should be directed to and will be fulfilled by the lead contact, Chao He (hechaochongqing@163.com).

Materials availability
This study did not generate new unique reagents.

Data and code availability
- Data reported in this paper will be shared by the lead contact upon request.
- This paper does not report original code. Existing code from our previous study was modified for current analyses. The modified version of this code is deposited and publicly available at Zenodo. The associated DOI is listed in the key resources table.
- Any additional information required to reanalyze the data reported in this paper is available from the lead contact upon request.

EXPERIMENTAL MODEL AND STUDY PARTICIPANT DETAILS

Wild-type C57/BL6 mice were purchased from the Army Medical University. Hcrt-Cre mice were used for fiber photometry, optogenetic, and chemogenetic experiments. GAD67-GFP (stock number: 007677) and PV-Cre (stock number: 008069) mice were purchased from the Jackson Laboratory. All mice were fed in the animal center of the Army Medical University with a 12/12 h light/dark cycle, an environmental temperature of $24 \pm 1\,°C$, and water and food ad libitum. Mice were housed in groups of 4–5, except for those with cannula, optical fiber, tetrode implants, and stereotactic injections, whom were housed individually. All the experiments were in line with the ethical requirements for animal care and use of the Army Medical University. All procedures were approved by the ethics committee of the Army Medical University.

METHOD DETAILS

Stereotactic injections and cannula implantation
We conducted stereotactic injections and cannula implantation in adult mice (8-12 weeks of age). After administering isoflurane anesthesia, the mice were gently secured on a stereotactic device (RWD Life Technology Co. Ltd.). Following disinfection with povidone-iodine and scalp incision, the skull's surface tissues were removed to expose it. With the aid of a microscope, small holes were drilled on both sides of the skull at the coordinates corresponding to the lateral hypothalamus (LH) (from bregma, anteroposterior (AP) = -1.58 mm, mediolateral (ML) = ±1.08 mm, dorsoventral (DV) = 4.75 mm) or the superficial layers of the MEC (from posterior fontanelle, AP = -0.20 mm, ML = ± 3.75 mm, DV = 2.00 mm) for virus injections. We utilized the Nanoject II (Drummond Scientific, USA) connected to a glass pipette for virus micro-injections. Once the pipette reached the target area, it was left in place for 2 minutes before injecting the virus at a speed of 13 nL/s with a 30-second interval. The pipette remained in the injection site for an additional 10 minutes before being slowly withdrawn.

For optogenetic and chemogenetic experiments, Cre-inducible AAV2/9-EF1α-DIO-ChR2-mCherry (Obio Technology Co. Ltd., China), AAV2/9-EF1α-DIO-NpHR3.0-eYFP (BrainVTA Technology Co. Ltd., China), AAV2/9-EF1α-DIO-hM3D-mCherry (BrainVTA Technology Co. Ltd., China), and AAV2/9-EF1α-DIO-hM4D-mCherry (BrainVTA Technology Co. Ltd., China) were bilaterally injected into the LH of the Hcrt-Cre mice, respectively, with a total volume of approximately 200 nL. To optogenetically inhibit PV$^+$ neurons in the MEC, AAV2/9-EF1α-DIO-NpHR3.0-eYFP (BrainVTA Technology Co. Ltd., China) was bilaterally injected into the MEC of PV-Cre mice with a total volume of around 200 nL. As controls, we injected Cre-inducible AAV2/9-EF1α-DIO-mCherry (BrainCase

Technology Co. Ltd., China) and AAV2/9-EF1α-DIO-eYFP (BrainVTA Technology Co. Ltd., China). For the photometry experiment, 200 nL of AAV2/9-EF1α-DIO-GCaMP6f (Obio Technology Co. Ltd., China) was injected into the LH of the Hcrt-Cre mice. To label the presynaptic terminals of glutamatergic neurons in the MEC, a mixture of AAV2/9-CaMKIIα-CRE (BrainVTA Technology Co. Ltd., China) and AAV2/9-hSyn-DIO-Synaptophysin-EGFP (BrainVTA Technology Co. Ltd., China) was unilaterally injected into the MEC with a total volume of approximately 200 nL.

For optogenetic manipulation and drug infusions, we implanted optical fibers (200 μm in diameter) (Inperstudio Alpha 8.2, Inper, China) and drug cannulas (L =5.00 mm, ID = 0.25 mm, RWD Life Science) in the superficial layers of the MEC (from posterior fontanelle, AP = -0.2 mm, ML = ± 3.75 mm, DV = 1.85 mm). We secured the optical fibers and drug cannulas to the skull using miniature screws (RWD Life Science Co., Ltd., China) and dental adhesive cement (Geristore A&B paste, DenMat).

Retrograde and anterograde tracing

Red retrobeads (500 nL, Lumafluor, 78R180) were injected into MEC in male wild-type mice (8-12 weeks of age) unilaterally (from posterior fontanelle, AP = -0.20 mm, ML = ± 3.75 mm, DV = -2.00 mm), CA1 (bregma, AP = -1.94 mm, ML = ± 1.40 mm, DV = -1.35 mm), CA2/3 (bregma, AP = -2.00 mm, ML = ± 2.50 mm, DV = -1.50 mm), DG (bregma, AP = -3.90 mm, ML = ± 2.80 mm, DV = -3.00 mm), VS (bregma, AP = -4.10 mm, ML = ± 3.37 mm, DV = -2.70 mm), PRH (bregma, AP = -4.60 mm, ML = ± 3.80 mm, DV = -0.50 mm), LEC (bregma, AP = -4.10 mm, ML = ± 4.25 mm, DV = -1.75 mm) via a glass cannula coupled to a 10 μL syringe. We manually injected red retrobeads slowly (about 5 minutes) and maintained position for 3 minutes after the infusion. 5-7 days after injection, coronal brain sections (40 μm) containing the LH and the MEC were collected for the immunofluorescence experiment.

To quantify the MEC-projecting Hcrt neurons, seven coronal sections of each red retrobeads-injected mouse containing the LH were collected from rostral to caudal. After Hcrt-A immunostaining, we quantified the total number of Hcrt neurons and retrobeads-labeled Hcrt neurons.

In the anterograde tracing experiments, AV2/9-EF1α-DIO-mCherry was injected into the LH of the male and female Hcrt-Cre mice (8-12 weeks of age). We quantified the axon fiber intensity of Hcrt neurons in the different subregions of the hippocampus and of the neighboring brain areas of the MEC by taking images with identical exposure time. Fluorescence values in these brain regions were analyzed by Image Pro Plus (Media Cybernetics, USA). The intensity of axonal terminals was calculated as the average optical density (AOD) of Hcrt fibers in the corresponding brain regions.

Behavioral tests

For the behavioral tests, male C57BL/6 mice (8-12 weeks of age) were used unless stated otherwise.

Object-place memory task

During the object-place memory task, test mice first underwent habituation in an empty contextual field with a yellow square, a red pentagram, a blue triangle, and a cyan circle cue on the four walls for 10 minutes. On the following day, two identical objects were placed in the familiar context. During the encoding stage, mice freely explored two identical objects (5 cm in diameter) for 5 minutes. After a 5-minute or 2-hour interval in the home cage, a 5-minute recall phase followed. In this recall phase, the spatial position of one object (object B) was changed, and mice were allowed to re-explore the two objects. Video recording was performed to record the exploration and re-exploration activities for further analyses.

Novel object memory test

In the novel object memory test, test mice were first habituated to an empty contextual field for 10 minutes. On the subsequent day, mice were allowed to freely explore two identical objects in the context for 5 minutes for memory encoding. After a 5-minute interval in the home cage, mice were allowed to re-explore the field for 5 minutes, during which time one of the objects was replaced by a novel object.

Mice were randomly assigned to distinct experimental conditions, and all behavior data were collected and analyzed by experimenters blind to the genotype and experimental conditions. The discrimination index was calculated using the formula: $T_m(B) - T_m(A) / T_m(B) + T_m(A)$,[83] where T_m represents the time spent exploring the respective objects. Mice with immobility time accounting for more than 80% during exploration were excluded from analyses, as reduced exploratory motivation could hinder effective spatial memory encoding.[84–86]

Closed-loop optogenetic intervention

For optogenetic activation of Hcrt fibers, we injected Hcrt-Cre mice with AAV-EF1α-DIO-ChR2-mCherry in the bilateral LH and implanted optical fibers in the superficial layers of the bilateral MEC. The optical fiber was connected to a 473 nm blue laser generator (Fiblaser Technology Co. Ltd., China), and the laser intensity at the tip of the optical fiber was adjusted to 15 mW under constant light. The illumination was controlled using a Master-8 waveform generator (AMPI, Israel). In both *in vivo* and *in vitro* light stimulation experiments, a 20 Hz laser pulse (10 ms) was applied.

For optogenetic inhibition of the LH_Hcrt-MEC pathway, we injected Hcrt-Cre mice with AAV-EF1α-DIO-NpHR3.0-eYFP in the bilateral LH and implanted optical fibers in the superficial layers of the bilateral MEC. In *in vivo* light stimulation experiments, constant light with an intensity of 10 mW was applied. To test whether the LH_Hcrt-MEC pathway is involved in object-place memory recall,

Neuron
Article

CellPress

optogenetic inhibition of LH_{Hcrt}-MEC pathway was performed at the recall stage. To prevent tissue overheating when stimulating NpHR3.0, a light on–off cycle of 8 s on and 2 s off was applied in both the male and female mice (8-12 weeks of age) based on the previous study.[77]

During encoding phase in the object-place memory task, a closed-loop system (Thinkerbiotech Co. Ltd., China) was utilized for real-time optogenetic intervention. Animal positions were monitored using an overhead infrared charge-coupled device (CCD) camera at a rate of 25 fps. We paired bilateral optogenetic intervention with times when the mouse's body center was less than 10 cm away from the center of the object. We focused on a subarea with the highest Ca^{2+} event density in Hcrt neurons based on a spatial distribution map of Ca^{2+} events we constructed.

Additionally, light-emitting diodes (LED) were installed on the head of the male and female mice (8–12 weeks of age), enabling specific head tracking and triggering of optogenetic interventions when the head entered a 3 cm region around the object's border.

Development and characterization of the $GRAB_{Hcrt0.5}$ sensor
The development, optimization, and characterization strategy of the $GRAB_{Hcrt0.5}$ sensors followed the methodology of our previous GRAB sensors. The $GRAB_{Hcrt0.5}$ sensors were cloned into a modified pDisplay vector (Invitrogen) for HEK293T cell expression or a pAAV vector using hSyn for AAV virus packaging.

For the transfection of cultured rat cortical neurons, AAV9 virus with a titer of approximately 5×10^{12} viral genomes (vg) ml^{-1} was added at day in vitro (DIV) 4. Cultured neurons were imaged using an inverted confocal microscope (Nikon) at DIV 11-16, equipped with a 20×/0.75 NA objective and a 10×/0.5 NA objective. A 488-nm laser and a 525/50-nm emission filter were used to collect $GRAB_{Hcrt0.5}$ sensor signals. HEK293T cells were cultured at 37 °C with 5% CO_2 in incubators. HEK293T cells were plated into CellCarrier-96 Ultra microplates (PerkinElmer) and imaged using the Opera Phenix high-content screening system (PerkinElmer) 24–36 h after transfection. A 488-nm laser and a 525/50-nm emission filter were used for imaging.

For the specificity characterization, we applied the following compounds at specified concentrations: glutamate (Glu), γ-aminobutyric acid (GABA), acetylcholine (ACh), norepinephrine (NE), dopamine (DA), serotonin (5-HT), histamine (HA), and adenosine (Ado) at 1 μM; corticotropin-releasing factor (CRF), somatostatin (SOM), vasoactive intestinal peptide (VIP), neurotensin (NTS), oxytocin (OT), arginine vasopressin (AVP), neuropeptide Y (NPY), substance P (SP), and cholecystokinin (CCK) at 10 μM.

In vivo fiber photometry
Three weeks after injecting AAV2/9-EF1α-DIO-GCaMP6f into the LH or AAV2/9-hSyn-$GRAB_{Hcrt0.5}$ into the MEC of the male mice (8-12 weeks of age), we implanted an optical fiber (diameter: 200 μm O.D., Inper, China) above the LH and secured it to the skull surface using dental cement. Mice were allowed to recover for an additional week in the home cage before fiber photometry recording. A commercialized fiber photometry system (Inperstudio Alpha 8.2, Inper, China) was used for fiber photometry recording. An optical fiber (200 μm in diameter, NA of 0.37, Inper, China) guided the 488 nm and 405 nm laser beams from the optical commutator to the implanted optical fiber. The power of the 488-nm imaging light was set at 30-40 μW, and the power of the 405-nm light was adjusted to approximately match the GCaMP6f or $GRAB_{Hcrt0.5}$ sensor fluorescence signals. The 405-nm channel served as an isosbestic control. Photomultiplier tubes collected and bandpass-filtered the fluorescence signals, which were then converted to voltage signals by an amplifier, further filtered through a low-pass filter, digitized at 20 Hz, and recorded by fiber photometry software (Inperstudio Alpha 8.2, Inper, China). We defined 2 s (-3 ∼ -1 s) windows before and after (1 ∼ 3 s) object-place exploration as pre-object-place exploration (Pre-OPE) and post-object-place exploration (Post-OPE), respectively, based on a previous study.[8] To detect the changes in Hcrt activity during animals' exposure to a novel environment with or without novel objects, the movement of the mice were tracked and the active exploration of the novel environment was defined as a movement state with running speed exceeded 2 cm/s.[61]

To construct the spatial distribution map of the strong Ca^{2+} signal of the Hcrt neurons, we used a sliding window with a length of 0.2 s and no overlaps between windows. The mean Ca^{2+} signal during one window period was computed and normalized by subtracting the mean signal of the full length from the mean signal of one window, then divided by the mean signal of the full length. Positive values reflecting strong Ca^{2+} events larger than the mean value were displayed. To visualize strong Ca^{2+} events at different locations, we tracked the centroid coordinates of the mice using in-house MATLAB code reported in a previous study[4] and calculated the median coordinates during one window period. We aligned the strong Ca^{2+} events to the coordinate series through the provided time of activity signal and used a heatmap to display the relative activity level of strong Ca^{2+} events at specific points in a two-dimensional space.

Multi-channel single-unit recording
For multi-channel single-unit recording, we used a custom-made electrode array consisting of tetrodes with four 23 μm nickel-cadmium wires (California Fine Wire) twisted together, each having an impedance of 100-250 kΩ. The electrode was slowly lowered into the MEC using a piezoelectric micromanipulator (SMX, Sensapex). Reference electrodes were fixed above the cerebellum with small stainless screws, and the electrode was firmly cemented on the animal's skull. The electrodes were connected to a 16-channel headstage (Neuralynx) with an amplifier for each wire and an LED for tracking the animal's position. This headstage was connected to a 2 m cable plugged into a commutator that allowed the animal to move freely during the behavioral task. The signals were amplified (Digital Lynx SX; Neuralynx, MO, USA) and acquired by Cheetah acquisition software (Cheetah 5.7.4). Units were amplified 10,000

times using a 16-channel amplifier (Neuralynx) and band-pass filtered at 300–10,000 Hz. Wild band signals were digitized at 30 kHz and band-pass filtered (0.1-9 kHz) by an amplifier (Digital Lynx SX; Neuralynx, MO, USA).

To investigate the effect of inhibiting the LH_{Hcrt}-MEC pathway on LFPs in the MEC during object-place exploration, we implanted a cannula surrounded by electrodes in the superficial layers of the left MEC, while a cannula without an electrode was implanted on the other side of the MEC in the male mice (8-12 weeks of age). After one week of recovery, the mice performed an object-place memory task, during which CNO-induced inhibition of the Hcrt terminals was applied in the bilateral MEC, and the local field potentials and units from the left MEC were acquired. A total of 11 and 13 mice with Hcrt neurons expressing mCherry and hM4D-mCherry were finally included in the data statistics in Figure 4C. 10 and 12 mice with Hcrt neurons expressing mCherry and hM4D-mCherry were shared in Figures 4C and 6. Two mice were excluded from electrophysiological data analyses in Figure 6 because there were incorrect electrode positions, despite the correct positions of the drug cannula implantation.

To explore the effect of PV$^+$ neurons on local field potentials in the MEC, we injected male PV-Cre mice (8-12 weeks of age) with AAV-EF1α-DIO-NpHR3.0-eYFP in the bilateral MEC. Three weeks later, optrodes were implanted in the superficial layers of the left MEC, with tetrode tips 0.5 mm longer than that of the optical fiber for efficient photostimulation of recorded neurons. After an additional week of recovery, local field potentials were recorded from the MEC in freely moving mice. A total of 9 and 7 mice with PV$^+$ neurons expressing eYFP and NpHR3.0 were finally included in the behavioral data statistics in Figure 5M. Three mice with PV$^+$ neurons expressing eYFP were excluded from electrophysiological data analyses in Figures 5G–5L because of the incorrect electrode positions, despite the optical fibers were located in the superficial layers of the MEC.

To confirm the efficiency of ChR2 and NpHR3.0, we implanted optrodes in the LH three weeks after injecting AAV-EF1α-DIO-ChR2-mCherry and AAV-EF1α-DIO-NpHR3.0-eYFP into the LH of the Hcrt-Cre mice, respectively. The neural activity from the LH was recorded one week after surgery. Light-activated neurons expressing ChR2 were identified based on a criterion consistent with a previous study.[9] Briefly, their latency from the onset of the light pulse was less than 10 ms, and other spikes were classified as spontaneous. The shape of the light-evoked spike waveform was similar to the spontaneous waveform of the same unit. The average firing rates during the 2 s preceding blue light stimulation were used as a baseline for comparison with the average firing rates during the stimulation of Hcrt neurons expressing ChR2-mCherry. To confirm the efficiency of NpHR3.0, constant light with an intensity of 10 mW was applied for 10 s. The average firing rates during the 10 s preceding yellow light stimulation were used as a baseline for comparison with the average firing rates during the stimulation of Hcrt neurons expressing NpHR3.0-eYFP.

Spike sorting and signal-to-noise ratio (SNR) calculation

Spike sorting was performed using SpikeSort3D 2.5.4. The first 3 principal components of the units were extracted and represented on a 3-dimensional plot. Waveforms with similar principal components were clustered using the KlustaKwik sorting method. The isolated cluster was regarded as a single-unit recorded from the same neuron. Cross-correlation histograms were used to eliminate cross-channel artifacts.

SNR was calculated following a previous study.[59] A small circular area surrounding the object location (radius of 3 cm around the border of the object) in the testing cage was marked as the object zone. Time points when the mouse's head was inside the object zone were classified as IN_{bin}, and the remaining frames were classified as OUT_{bin}. We recorded the spikes of neurons corresponding to the IN_{bin} and OUT_{bin} position frames. For all recorded neurons, the firing probability for IN_{bin} (mIN_{bin}) and OUT_{bin} ($mOUT_{bin}$) frames was calculated. We also calculated the standard deviation ($SDOUT_{bin}$) of the neuronal activity in OUT_{bin} frames. The signal-to-noise ratio of each neuron was estimated using the following equation:

$$SNR = (mIN_{bin} - mOUT_{bin}) / SD_{OUTbin}$$

Local field potential analysis

We calculated the spectrum of the local field potential using the Multi-Taper method, as described in detail in a previous study.[4] In brief, NeuroExplorer software (version 5.0) was used to analyze the power spectral density with the multitaper method (number of tapers = 3, Time-bandwidth product = 3). The relative power of theta (4–12 Hz) or gamma (25–120 Hz) oscillations was computed by dividing the area under the spectrum at that frequency by the total area under the spectrum.

Identification of the recording sites

After completing the collection of electrophysiological data, we anesthetized the mice with isoflurane and applied a direct current of 0.01 mA for 10 second via the electrode for electrolytic lesion. Subsequently, the mice were transcardially perfused with saline followed by 4% paraformaldehyde. The brains were removed and placed in a dehydration solution containing 30% sucrose and 4% paraformaldehyde. Continuous frozen sections of the MEC were cut and stained with 4',6-diamidino-2-phenylindole (DAPI) for the identification of the recording sites. Any mice with incorrect recording sites were excluded from the analyses.

Whole-cell patch clamp recordings

The procedures for whole-cell patch clamp recordings were similar to those described in previous studies.[7,87] After anesthetizing the mice with isoflurane, the brain was rapidly removed and placed in ice-cold section solution saturated with 95% O_2 and 5% CO_2. The section solution consisted of 220 mM sucrose, 10 mM glucose, 2.5 mM KCl, 1 mM $CaCl_2$, 26 mM $NaHCO_3$, 6 mM $MgCl_2$, and 1.25 mM NaH_2PO_4. The brain was then cut into horizontal slices containing the MEC with a thickness of 400 μm in the ice-cold section solution using a VT1000 tissue slicer (Leica, Germany). Subsequently, the slices were incubated for 1 hour in oxygen-saturated artificial cerebrospinal fluid (ACSF) containing 2.5 mM KCl, 125 mM NaCl, 2 mM $CaCl_2$, 26 mM $NaHCO_3$, 1.3 mM $MgSO_4$, 1.25 mM

Neuron
Article

CellPress

NaH$_2$PO$_4$, and 20 mM glucose at room temperature. The brain slices were then moved into a submerged chamber for recording with continuous infusion of oxygen-saturated ACSF.

The targeted neurons were identified using an upright fluorescent microscope (Olympus, Japan) equipped with differential contrast optics and an infrared video imaging camera. Whole-cell recordings were performed on the target neurons in the superficial layers of the MEC using glass pipettes containing the solution (130 mM potassium gluconate, 5 mM KCl, 2 mM MgCl$_2$, 10 mM HEPES, 0.1 mM EGTA, 2 mM Na$_2$-ATP, 0.2 mM Na$_2$-GTP). For recording inhibitory synaptic currents, a special pipette solution containing 145 mM CsCl, 10 mM HEPES, 2 mM MgCl$_2$, 1 mM EGTA, and 2 mM ATP was prepared. After clamping the targeted neurons at -60 mV with stable recording for at least 15 minutes, we injected step currents (delta current = 20 pA, duration = 1 s) into the clamped neurons to induce voltage curves and action potentials. Different neuronal types were distinguished based on the morphological and electrophysiological properties of these neurons, as described in previous studies.[56,88] GFP-positive interneurons were further classified into PV$^+$ and SOM$^+$ neurons. PV$^+$ neurons exhibited spike firing exceeding 60 Hz without adaptation, while SOM$^+$ neurons showed prominent hyperpolarizing sag and spike adaptation. GFP-negative neurons were classified as excitatory glutamatergic neurons, characterized by larger somata and smaller fast after-hyperpolarization potential. Following 15 minutes of baseline recording, we bath-applied Hcrt-A (Tocris) for 2 minutes with a speed of approximately 2 mL/min, followed by a 30-minute washout period. The average values of the 2 min before drug administration were used as baseline. We excluded a neuron from data analysis if the change in series resistance was larger than 25 MΩ or 15% of the baseline.

The on-line electrophysiological data were continuously recorded using an EPC10 recording system and the Patchmaster software (HEKA, Germany). The electrical signals were processed with a 4 KHz low-pass filter and digitized at 10 kHz. The off-line data were analyzed using Igor Pro v.4.03 (WaveMetrics) or MiniAnalysis Program 6.0 (Synaptosoft). For isolating spontaneous or miniature excitatory postsynaptic currents (sEPSCs or mEPSCs), we continuously infused GABA$_A$R antagonist picrotoxin (PIC, 100 μM) or sodium channel blocker tetrodotoxin (TTX, 1 μM) + Picrotoxin (PIC, 100 μM) into the ACSF, respectively. For recording spontaneous or miniature inhibitory postsynaptic currents (sIPSCs or mIPSCs), we used a special pipette solution containing CsCl and administrate the AMPA receptor antagonist CNQX (10 μM) and NMDA receptor antagonist AP-5 (50 μM) or TTX (1 μM) + CNQX (10 μM) + AP-5 (50 μM) into the ACSF throughout the recording, respectively. On some occasions, we clamped membrane potentials at +10 mV to record the SIPSCs in the excitatory glutamatergic neurons without a general blockade of excitatory synaptic transmission (V$_m$ of +10 mV is closed to the reversal potential of ionotropic glutamate receptors. In this case, the SIPSC amplitude is maximized with the minimization of the SEPSCs in the recorded neuron). The events of spontaneous or miniature postsynaptic currents with rapid onset and characteristic kinetics of exponential decay were first automatically detected by the MiniAnalysis software with pre-set parameters, and then re-checked with manual verification. The frequency and amplitude of the postsynaptic currents before and after drug infusion were calculated.

In double-patch experiments, we simultaneously clamped a pair of neurons with a distance of less than 40 μm. First, we injected step currents (-300 pA to +300 pA, delta current = 100 pA, duration = 1 s) into those neurons to identify the neuronal types. When recording a pair of glutamatergic and GABAergic neurons, we selected stimulation parameters that could induce 8-16 action potentials (1 s) in the excitatory cell and recorded the excitatory postsynaptic currents (EPSCs) in the GABAergic neuron. Only the EPSCs with a latency less than 2.4 ms and a signal-to-noise ratio higher than 2 were considered as the direct synaptic response, and these currents were referred to as unitary EPSCs (uEPSCs).[56] When reliable uEPSCs could be evoked, this pair of neurons was considered to have a direct monosynaptic connection. The uEPSCs at baseline and during drug infusion were recorded. The response reliability, defined as the ratio of the number of evoked uEPSCs in the postsynaptic neuron to the number of corresponding action potentials in the presynaptic neurons, and the amplitude of the uEPSCs were calculated for comparison. On some occasions, we also recorded a pair of excitatory cells. We induced 8-12 action potentials (1 s) in one of these cells and recorded the evoked postsynaptic currents in the other cell. According to the above-mentioned criteria, the postsynaptic current was judged whether it was a unitary or spontaneous postsynaptic current, and the connectivity percentage between glutamatergic neurons and GABAergic neurons was calculated.

For the optical stimulation of the Hcrt neuron terminals in the MEC, AAV-EF1α-DIO-ChR2-mCherry viruses (Obio Technology Co. Ltd., China) were bilaterally injected into the LH of adult Hcrt-Cre mice. After about four weeks of virus expression, PV$^+$ neurons were recorded from horizontal brain slices containing the MEC, prepared according to the above-mentioned method. To investigate the role of endogenous Hcrt in the excitability of PV$^+$ interneurons in the MEC, we recorded the membrane potentials and spontaneous firing of PV$^+$ interneurons under the current clamp configuration. After obtaining a stable baseline recording, 473 nm blue light (20 Hz, 10 ms, 10 mW under constant light) was delivered via an optical fiber placed above the recorded cell. To evaluate the potential physiological significance of endogenous Hcrt on excitatory synaptic transmission, we isolated sEPSCs from PV$^+$ interneurons with continuous infusion of the GABA$_A$R antagonist PIC (100 μM). After recording the sEPSCs for about 3 minutes, we applied 473 nm blue light pulses to stimulate the endogenous Hcrt release, followed by a washout period. The average values of the 1 min before optogenetic stimulation were used as baseline for comparisons.

To verify whether CNO could silence hM4D-mCherry Hcrt neurons, AAV9-EF1α-DIO-hM4D-mCherry viruses (BrainVTA Technology Co. Ltd., China) were bilaterally injected into the LH of male Hcrt-Cre mice (8-12 weeks of age). After about four weeks of recovery, coronal brain slices containing the LH were prepared. Action potentials in hM4D-mCherry Hcrt neurons were elicited by depolarizing the membrane potential in the current clamp configuration. After recording the baseline for about 5 minutes, CNO (5 μM) was bath-applied for 2 minutes. The average values of the 2 min before CNO administration were used as baseline for comparisons.

Intraperitoneal injection and cannula infusion of drugs

For chemogenetic activation of the Hcrt neurons, we administered Clozapine N-oxide (CNO, Tocris Biosciences, 4936) via intraperitoneal injection at a concentration of 1 mg/kg before behavioral assays. In cannula microinjection experiments, we infused CNO (5 μM) in a total volume of 500 nl per side at a speed of 250 nl/min through an injector cannula using a microinfusion pump (Harvard Apparatus). Suvorexant (50 μM, Abmole, M2272) was also administered via microinjections at the same speed in a total volume of 200 nl. The injection infusers were removed 2 minutes after completion of the infusion.

Immunohistochemistry

Male mice (8–12 weeks of age) were anesthetized with isoflurane and then transcardially perfused with 60 mL of physiological saline followed by 60 mL of 0 °C, 4% paraformaldehyde (PFA) in phosphate buffer (PBS). We extracted the brains and fixed them with 4% PFA in PBS for 6 hours, followed by 0 °C, 30% sucrose overnight for dehydration. After that, we obtained brain sections using a freezing microtome. Slices containing the MEC or LH were collected and preserved in the PBS solution for immunohistochemical staining.

To detect the expression of Hcrt-A and c-Fos, we washed the slices containing the MEC and other brain areas (25 μm) with PBS three times (5 minutes each time). Then, we incubated the slices in a blocking solution with 0.1% Triton X-100 and 5% donkey serum at 37°C for 30 minutes. Next, the slices were incubated with primary antibodies in an incubation solution at 4°C for 48 hours. After being washed with PBS three times (5 minutes each time), the slices were incubated in the incubation solution containing the secondary antibodies at room temperature for 3 hours. Finally, the slices were incubated with 0.01% DAPI for 5 minutes at room temperature for staining the nuclei. After being washed with PBS three times (5 minutes each time), the slices were mounted, dried, and then investigated with confocal microscopy (Carl Zeiss, Jena, Germany).

To investigate whether ChR2-mcherry, hM3D-mcherry, hM4D-mcherry, and GCaMP6f were specifically expressed in the Hcrt neurons and the distribution of Hcrt-positive fibers, we prepared slices containing the LH and hippocampal-entorhinal region (40 μm). The procedures for immunohistochemical staining were the same as mentioned above, except that we used the primary antibody anti-goat Hcrt-A (1:500, Santa Cruz, SC-8070), and the secondary antibodies including Alexa Flour 568 donkey anti-goat IgG (1:500, Invitrogen), Alexa Flour 488 donkey anti-goat IgG (1:500, Invitrogen), and Alexa Flour 647 donkey anti-goat (1:500, Invitrogen).

To detect c-Fos expression, we used the primary antibody anti-rabbit c-Fos (1:1000, Millipore, ABE457), and the secondary antibody Alexa Flour 488 donkey anti-rabbit (1:800, Invitrogen). For the quantification of c-Fos positive neurons in the entorhinal cortex and hippocampus, we further fit the images with the mouse brain atlas of Paxinos and Franklin to determine the boundaries of each subregion. The number of c-Fos positive neurons and intensity of the Hcrt neuron fibers were analyzed using ImageJ software.

Immune electron microscopy

Male mice (8-12 weeks of age) were anesthetized with an intraperitoneal injection of sodium pentobarbital (50 mg/kg) and then transcardially perfused with 20 mL of physiological saline followed by 40 mL of 0 °C 4% PFA containing 0.05% glutaraldehyde. Brains were extracted and fixed with 4% PFA containing 0.05% glutaraldehyde at 4°C for 12 hours. We obtained horizontal slices containing the superficial layers of the MEC with a thickness of 45 μm by continuous section of the brain tissues with a vibratome. The slices were blocked in a blocking solution containing 2.5% BSA and 0.05 % Triton at room temperature for 2 hours. After being washed with PBS for 30 minutes, the slices were incubated in the primary antibody diluent (anti-goat HcrtR1 (1:100, Origene, TA303362); anti-rabbit GABA (1:500, Sigma-Aldrich, A2052)) containing 1% BSA and 0.05% Triton on the shaking table at room temperature overnight. We prepared secondary antibodies for HcrtR1 and GABA using the colloidal gold method and DAB method, respectively. After being washed with PBS for 30 minutes, the slices were incubated with the secondary antibodies on the shaking table at room temperature overnight. The slices were washed with PBS for 30 minutes and then fixed with 2% glutaraldehyde for 1 hour. After a 30-minute PBS wash, the slices were washed with deionized water twice, treated for silver enhancement at room temperature for 20 minutes in the dark, and then washed with deionized water twice and PBS for 10 minutes, followed by DAB staining for 10 minutes. After that, the slices were washed with PBS for 40 minutes, and then fixed with osmic acid at room temperature for 2 hours. We conducted gradient alcohol (50%, 70%, 85%, 90%, and 95% with 3 minutes each time) dehydration for the slices, and then the slices were treated with absolute ethyl alcohol three times (4 minutes each time) and acetone for three times (4 minutes each time). The slices were placed in the mixture of acetone and resin with a ratio of 1:1 and put in the 33°C oven overnight. After being med in the resin, the slices were put in the 42°C oven for 3 hours. Lastly, we performed the ultrathin section for each slice, followed by observation under the transmission electron microscope.

Histological identification

After completing the behavioral tests, we anesthetized the mice with isoflurane and transcardially perfused them with saline, followed by 4% paraformaldehyde. We then took out the brains and placed them in a 30% sucrose and 4% paraformaldehyde solution for dehydration. We prepared frozen sections of the MEC or LH and stained them with DAPI for the identification of the location of optical fibers or cannulae. We included only the animals in which the tips of optical fibers and cannulae were located in the superficial layers of the MEC or the LH for data analyses.

Neuron
Article

🦋 **CellPress**

QUANTIFICATION AND STATISTICAL ANALYSIS

All the statistical analyses were performed using SigmaPlot 12.5. Data were shown as mean ± S.E.M. unless otherwise stated. We formally tested normality and equal variances for each group of data. For data with normal distribution and equal variances, we performed one-sample t-test, paired or unpaired t-test, analysis of variance (ANOVA) with post hoc Fisher LSD test, and repeated measures ANOVA with post hoc Fisher LSD test for comparisons between groups. For data that did not conform to the normal distribution or equal variances, we performed non-parametric tests. Significant differences were accepted when $P < 0.05$. $*P < 0.05$. $*nP < 0.05$. $*noP < 0.05$.